

**UCLA**

**UCLA Previously Published Works**

**Title**

Kinematic Response Functions and Dynamic Stiffnesses of Bridge Embankments

**Permalink**

<https://escholarship.org/uc/item/4rf9x53s>

**Journal**

Earthquake Engineering and Structural Dynamics, 31(11)

**Authors**

Zhang, Jian

Makris, Nicos

**Publication Date**

2002

Peer reviewed

# KINEMATIC RESPONSE FUNCTIONS AND DYNAMIC STIFFNESSES OF BRIDGE EMBANKMENTS

JIAN ZHANG<sup>1</sup> and NICOS MAKRIS<sup>2</sup>

*Department of Civil and Environmental Engineering, U. C. Berkeley, CA 94720*

## SUMMARY

Recognizing that soil-structure interaction affects appreciably the earthquake response of highway overcrossings, this paper compares approximate analytical solutions and finite element results to conclude on a simple procedure that allows for the estimation of the kinematic response functions and dynamic stiffnesses of approach embankments. It is shown that the shear-wedge model yields realistic estimates for the amplification functions of typical embankments and reveals the appropriate levels of dynamic strains which are subsequently used to estimate the stiffness and damping coefficients of embankments. The shear-wedge model is extended to a two-dimensional model in order to calculate the transverse static stiffness of an approach embankment loaded at one end. The formulation leads to a sound closed-form expression for the critical length,  $L_c$ , that is the ratio of the transverse static stiffness of an approach embankment and the transverse static stiffness of a unit-width wedge. It is shown through two case studies that the transverse dynamic stiffness (“spring” and “dashpot”) of the approach embankment can be estimated with confidence by multiplying the dynamic stiffness of the unit-width wedge with the critical length,  $L_c$ . The paper concludes that the values obtained for the transverse kinematic response function and dynamic stiffness can also be used with confidence to represent the longitudinal kinematic response function and dynamic stiffness respectively.

KEY WORDS: bridge embankment, seismic response, kinematic response function, dynamic stiffness.

## INTRODUCTION

Over the last thirty years several highway overcrossings have experienced severe damage under strong ground shaking. Most of this damage was the result of excessive seismic displacements and deflections that have been substantially underestimated during design. Such design deficiencies appear to be the result of dated design concepts, which typically considered a small fraction of the actual forces and displacements that develop on bridges during strong earthquake

---

1. Graduate Student Researcher

2. Associate Professor

shaking. A direct consequence of the underestimated seismic displacements, which were the combined result of poor representation of the kinematic characteristics of the ground, low lateral forces, and overestimated stiffnesses, was that the seating length at the deck supports was unrealistically short and the lateral separations between adjacent structures were typically inadequate, resulting in loss of support or pounding (Maragakis and Jennings 1987). These geometrical inconsistencies resulted in spectacular failures that have been witnessed during the recent 1989 Loma Prieta and the 1994 Northridge earthquakes in California and the 1995 Kobe earthquake in Japan. In addition to failures that are the result of geometric inconsistencies (limited seating length, pounding-abutment slumping), several bridges failed due to inadequate strength and ductility in their columns, cap-beams, and foundations (Priestley et al. 1996).

In view of these failures, many research programs were launched after the 1971 San Fernando earthquake to study the seismic resistance of highway bridges. Improvements have been achieved in both design and analysis of bridge structures with the help of strong-motion records. Extensive retrofit programs have been implemented in California, which include jacketing of columns and the use of composite materials (FHWA 1995).

An alternative strategy for the seismic protection of bridges that the California Department of Transportation (Caltrans) is currently investigating is the implementation of devices such as isolation bearings and supplemental dampers. Several bridges worldwide are equipped with seismic protection devices (Skinner et al. 1993). The increasing need for safer bridges in association with the rapid success of seismic protection devices in buildings has accelerated the implementation of large-capacity damping devices in bridges (Delis et al. 1996). Typically bridges and, in particular, freeway overcrossings are more sensitive than buildings to soil-structure interaction, yet the potentially important effects of soil-structure interaction are often downplayed or occasionally neglected even in relatively sophisticated studies that consider the implementation of modern technologies.

Wilson and Tan (1990a) was the first study that presented a simple analytical model to estimate the static transverse and vertical stiffnesses of approach embankments of typical short- and medium-span highway bridges. Their closed-form expressions that account for the sloped geometry of the embankment provide a realistic estimate of the static stiffnesses of a unit-width wedge and are consistent with the shear-wedge model that can be easily used to estimate the amplification functions of approach embankments. Their study, however, did not provide any information on the embankment stiffnesses along the longitudinal direction nor any information on the

embankment damping in any direction. Furthermore, in their companion paper (Wilson and Tan 1990b) while initial calculations resulted in a soil shear modulus as low as  $G = 2.4MPa$ , subsequent values of the embankment stiffnesses are calculated using a shear modulus value as high as  $G = 7.2MPa$  (three times larger). In this paper, the concept of the shear-wedge model established by Wilson and Tan (1990a,b) is utilized to develop kinematic response functions and dynamic stiffnesses (stiffness and damping) of the approach embankments. A dependable estimation of the crest response not only allows for a more appropriate support motion at the end abutments but also reveals realistic levels of dynamic strains which are subsequently used to estimate the stiffness and damping coefficients of embankments. The shear-wedge model is extended to a two-dimensional model in order to calculate the transverse static stiffness of an approach embankment loaded at one end. The formulation reveals a sound closed-form expression for the critical length,  $L_c$ , that is the ratio of the transverse static stiffness of an approach embankment and the transverse static stiffness of a unit-width wedge.

### **CONSIDERATIONS FOR RESPONSE ANALYSIS**

It is well known from experimental studies (Romstad et al. 1995) and theoretical considerations (Siddharthan et al. 1997, among others) that the behavior of bridge abutments is increasingly nonlinear as displacements increase. Nevertheless, analytical studies on recorded motions have indicated that even under strong earthquake motion the force-displacement loops of bridge abutments resemble elliptical shapes (Goel and Chopra 1997). Earlier studies that were based on a system identification methodology indicated that linear models provide a good fit with the measured response of a bridge (Werner et al. 1987). Such observations indicate that even for the design earthquake an equivalent linear analysis can provide dependable estimates of the bridge response.

Strong-motion records near and on highway overcrossings revealed that the crest motion of the approach embankment can be more than two times the motion recorded near the pile cap of the center bent (Maroney et al. 1990), indicating that the kinematic response of embankments might have a substantial effect on the bridge response. No established procedures are presently available to account for this amplification. Current design procedures used by Caltrans (1989) assume only an equivalent linear distributed spring to approximate the flexibility of the embankment without considering the energy absorbed by the embankment and the overall dynamic nature of the problem. It becomes apparent that when the evaluation of displacements is of prime interest, a more detailed analysis is needed, since it has been stressed by several researchers that the

effect of soil-structure interaction is increasingly important as the intensity of the ground shaking increases.

The numerical study presented herein is conducted within the context of equivalent linear viscoelasticity and is based on a three-dimensional (3-D) finite element analysis that is partly used to validate the dependability of approximate transfer functions and dynamic stiffnesses computed with the shear-wedge model and its extension. The proposed transfer functions, springs and dash-pots, are expected to improve the estimation of displacements and forces that develop at the end abutments. It is shown that the presented formulation provides realistic estimates of the response even under larger abutment displacements when the soil of the embankment is strained in the non-linear range.

### **KINEMATIC RESPONSE FUNCTIONS**

The approach earth embankments on many highway overcrossings usually have a length that is several times larger than the dimension of the trapezoidal cross section of the embankment. Typical approach embankments of highway overcrossings extend 150 m or more beyond each end abutment of the bridge. Because of this geometry several researchers have adopted a two-dimensional (2-D) plane-strain idealization to derive approximate response quantities.

#### *The Shear Beam Approximation*

Sixty years ago, Mononobe (1936) was perhaps the first to consider that earth dams and embankments are deformable bodies, and introduced the ingredients of what has come to be called the “shear-wedge” or the “shear-beam” model. This concept has served as the basis for many of the newly developed models and has been revisited in detail in the review paper by Gazetas (1987). In this section the shear-wedge or the shear-beam model is discussed briefly to show the advantages and limitations of a one-dimensional (1-D) approximation when applied to three-dimensional approach embankments.

Figure 1 (top) represents the cross section of an infinitely long embankment subjected to a horizontal rigid-base excitation,  $\ddot{u}_g$ , under the condition of plane strain deformations. Assuming that only horizontal shearing deformations develop and that horizontal displacements are uniform across the embankment (i.e.  $u_x(z, t)$  are independent of  $x$ ), the dynamic equilibrium of a slice of the embankment gives

$$\rho_s \frac{\partial^2}{\partial t^2} [u_x(z, t) + u_g(t)] = \frac{1}{z} \frac{\partial}{\partial z} \left( G_s(z) \cdot z \cdot \frac{\partial}{\partial z} u_x(z, t) \right) \quad (1)$$

where  $\rho_s$  and  $G_s(z)$  are the density and the shear modulus of the soil material of the embankment. In general the shear modulus,  $G_s(z)$ , is a function of  $z$ . For instance, a reasonable assumption is to assume that  $G_s(z)$  is proportional to the square root of the confining pressure (Dakoulas and Gazetas 1985). In this study the shear modulus of the embankment has been assumed to be a constant.

Under free vibrations ( $u_g(t) = 0$ ), the solution of equation (1) gives the free vibration characteristics of the shear-wedge. The natural frequencies,  $\omega_n$ , are given by

$$\omega_n = k_n V_s \quad (2)$$

where  $V_s = \sqrt{G_s/\rho_s}$ , is the shear-wave velocity of the soil material and  $k_n$  is the  $n$ th wave number that is obtained from the solution of the characteristic equation

$$J_0[k_n(z_0+H)]Y_1(k_n z_0) - J_1(k_n z_0)Y_0[k_n(z_0+H)] = 0 \quad (3)$$

The value of the constant  $z_0$  depends on the geometry of the embankment. In the general case of an unsymmetrical embankment,  $z_0 = B_c H / (B_b - B_c)$ ; whereas in the case of a symmetric embankment with slope  $S$ ,  $z_0 = S B_c / 2$ .  $B_c$  and  $B_b$  are the crest and bottom width respectively and  $H$  is the height of the embankment. The geometrical characteristics of two approach bridge embankments of interest, which have been instrumented and subjected to strong shaking are shown in Figure 1 (bottom). In equation (3)  $J_0$ ,  $J_1$ ,  $Y_0$ , and  $Y_1$  are the zero- and first-order Bessel functions of the first and second kind respectively (Abramowitz and Stegun 1970). The mode shapes are given by

$$\phi_n(z) = J_0(k_n z)Y_1(k_n z_0) - J_1(k_n z_0)Y_0(k_n z) \quad (4)$$

When the ground input in (1) is a harmonic motion,  $u_g(t) = u_{g0} e^{i\omega t}$  of frequency  $\omega$ , equation (1) can be solved analytically. The quantity of interest is the ratio of the amplitude of the crest motion,  $|u_x(z_0) + u_g|$ , to the amplitude of the base motion,  $u_g$ . This transfer function is the kinematic response function of the shear wedge and is given by

$$|I(\omega)| = \left| 1 + \frac{u_x(z_0)}{u_{g0}} \right| = \left| \frac{c_1 J_0(kz_0) + c_2 Y_0(kz_0)}{u_{g0}} \right| \quad (5)$$

where  $k = \omega/V_s$ .  $c_1$  and  $c_2$  are integration constants given by

$$c_1 = \frac{u_{g0}}{J_0(k(z_0+H)) - \frac{J_1(kz_0)}{Y_1(kz_0)} Y_0(k(z_0+H))} \quad (6)$$

$$c_2 = -\frac{J_1(kz_0)}{Y_1(kz_0)}c_1 \quad (7)$$

In the case where the soil is assumed as a purely elastic material, its shear modulus is real and the kinematic response function given by (5) is singular at all natural frequencies given by (2). In reality soil material has internal damping and the kinematic response function is finite along the entire frequency spectrum. Experimental studies in the 1960s indicated that the storage and loss modulus of sand is nearly frequency independent (Hardin 1965). Following Hardin's pioneering work it has become a practice to use the following simple expression of the dynamic modulus of soil materials

$$G(\omega) = G_1 + iG_2 \text{sgn}(\omega) = G_1(1 + i\eta \text{sgn}(\omega)) \quad (8)$$

where  $G_1$  and  $G_2$  are frequency independent quantities and  $\omega$  is the frequency variable. The signum function  $\text{sgn}(\omega)$  is appended at the imaginary part of (8) so that the loss modulus of the proposed model is an odd function of frequency. This condition ensures that under a real valued strain history,  $\gamma(t)$ , with Fourier transform,  $\gamma(\omega) = \int_{-\infty}^{\infty} \gamma(t)e^{-i\omega t} dt$ , the resulting stress history

$$\tau(t) = \frac{1}{2\pi} \int_{-\infty}^{\infty} (G_1 + iG_2 \text{sgn}(\omega)) \gamma(\omega) e^{i\omega t} d\omega \quad (9)$$

is real valued. Since the real part,  $G_1$  (storage modulus) in (8) is frequency independent it assumes the static value of the shear modulus of the material  $G_s$ ; whereas the constant,  $\eta = G_2/G_1$ , appearing in (8) is the hysteretic damping coefficient. Accordingly the constant hysteretic model has been traditionally expressed as  $G(\omega) = G_s(1 + i\eta \text{sgn}(\omega))$ , where  $G_s$  and  $\eta$  are strongly strain dependent. Figure 2 plots selected curves published in the literature based on the work of Seed and Idriss (1970), Iwasaki et al. (1978), Tatsuoka et al. (1978), Vucetic and Dobry (1991), among others. The darker line on Figure 2 represents an averaged curve of these reported curves, and is the curve used for iteration in this paper. Note that in the bottom of Figure 2 the material damping of soil is presented in terms of  $\eta = G_2/G_1$  and not in terms of the modal damping of the embankment,  $\xi_n$ . It should be noted that the constant hysteretic model given by (8) is a pathological model since it does not possess a real-valued constitutive law in the time domain. The main flaw of this model that is due to its noncausality is well known to the literature (Caughey 1962; Crandall 1963, 1970; Inaudi and Kelly 1995) and has been rigorously addressed by Makris (1997) and Makris and Zhang (2000). Despite its noncausal behavior the constant hys-

teretic model given by (8) is a reliable model for the dynamic analysis of earth structures, in particular when the excitation has several cycles.

Using the correspondence principle (Flugge 1975) the harmonic response of an embankment that consists of viscoelastic material is given from the same equations that are derived by assuming a purely elastic material after replacing the real shear modulus,  $G_s$ , with the complex shear modulus  $G_s(1 + i\eta \text{sgn}(\omega))$ . With this substitution the shear-wave velocity,  $V_s$ , and natural frequencies,  $\omega_n$ , become complex quantities. As an example, the modal frequencies,  $\omega_n$ , are given by

$$\omega_n = k_n \sqrt{\frac{G_s}{\rho_s}} \cdot \sqrt{1 + i\eta} \quad (10)$$

in which  $k_n$  is again the  $n$ th wave number that is obtained from the solution of the characteristic equation (3). The modal damping ratio,  $\xi_n$ , is given by

$$\xi_n = \frac{\text{Im}\{\omega_n\}}{\sqrt{(\text{Re}\{\omega_n\})^2 + (\text{Im}\{\omega_n\})^2}} \approx \frac{\eta/2}{1 + \eta^2/8} \approx \frac{1}{2}\eta \quad (11)$$

It is important to emphasize that the modal damping ratio,  $\xi_n$ , appearing on the left of equation (11), is a quantity that characterizes the modal damping of the entire soil embankment; whereas, the hysteretic damping coefficient,  $\eta = G_2/G_1$ , appearing on the right of (11), characterizes the dissipation of the soil material at a point. It is partly because of the simple relation given by (11) that the modal damping ratio and the hysteretic damping coefficient are often confused in the literature without distinguishing between the modal damping ratio of an entire structure,  $\xi_n$ , and the loss factor,  $\eta$ , of a viscoelastic material.

In selecting the values of  $G$  and  $\eta$  iterations are required, since their values are strain dependent and the strain level is not known a priori. Initially, a strain level is projected, the associated shear modulus and damping coefficient are estimated, and response time histories are computed. Seed and Idriss (1969) suggested that two thirds of the response strain should be used as the average strain to evaluate  $G(\gamma)$  and  $\eta(\gamma)$  for the next iteration. With a finite element analysis different values of soil parameters can be assigned at various locations according to local strain level (Idriss et al. 1974). With the shear-wedge formulation only a macroscopic value of an average strain  $\hat{\gamma} = \hat{u}_x^c/H$  can be evaluated, where  $\hat{u}_x^c$  is some representative crest displacement (say  $\hat{u}_x^c = \frac{2}{3}u_{x,max}^c$ ) and  $H$  is the height of the shear wedge.



The shear-wedge model presented in the previous section is a one-dimensional approximation of a three-dimensional structure. In this section the solution of the shear-wedge approximation is compared with the results of a 2-D and 3-D finite element analysis. The computer software ABAQUS (1997) is used in this study to conduct free- and forced- vibration dynamic analyses of the embankment. In the 2-D formulation isoparametric elements were used, whereas in the 3-D analysis eight node solid elements were used. The approach slope along the longitudinal direction is included in the 3-D model.

The response is computed in the time domain where damping is approximated with the Rayleigh approach. The damping matrix,  $[C]$ , of the soil structure is assumed to be a linear combination of the mass matrix,  $[M]$ , and the stiffness matrix,  $[K]$

$$[C] = \alpha[M] + \beta[K] \quad (12)$$

in which  $\alpha$  and  $\beta$  are frequency-independent coefficients. With this ad hoc approach the elements of the damping matrix,  $[C]$ , can be constructed by using the information on the modal damping of the soil structure at two distinct modes

$$\xi_j = \frac{\eta}{2} = \frac{1}{2} \left( \frac{\alpha}{\omega_j} + \beta \omega_j \right) \quad (13)$$

At every iteration where the new strain level is established and the values of  $G$  and  $\eta$  are updated, new values of the parameters  $\alpha$  and  $\beta$  are established. In this analysis the values of  $\alpha$  and  $\beta$  were computed by using the first and second modal frequencies ( $j = 1$  and  $j = 2$ ).

Figure 3 plots the computed time histories of the converged strains at the base, mid-height and crest of the north embankment of the Meloland Road Overcrossing subjected to the 1979 Imperial Valley earthquake (free-field records). The left column plots the time history of strains due to transverse shearing ( $\gamma_{xz}$ ), the center column plots the time history of strains due to longitudinal shearing ( $\gamma_{yz}$ ), whereas the right column plots the amplitude of the maximum shear strains as a function of time. Following the Seed and Idriss suggestion, Figure 3 indicates that an appropriate value for the converged strain is  $\hat{\gamma} \approx 9.4 \times 10^{-3}$ . This corresponds to  $G = 1.5 \text{ MPa}$  ( $G/G_{max} \approx 0.08$ ), and  $\eta \approx 0.56$ .

Figure 4 plots the converged strain histories at the west embankment of the Painter Street Bridge subjected to the 1992 Petrolia earthquake (free-field records). In this case the converged

strain level is smaller than the strain level shown in Figure 3, to a value of  $\hat{\gamma} \approx 3.2 \times 10^{-3}$ . The equivalent linear values for the stiffness and damping coefficient adopted are  $G = 9.4 \text{ MPa}$  ( $G/G_{max} \approx 0.16$ ), and  $\eta = 0.48$ .

Once the converged strains have been established they can be integrated in the time domain to yield the displacement profile of the embankment. In the special case of a harmonic steady-state excitation,  $\ddot{u}_g = \ddot{u}_{go} e^{i\omega t}$ , the software ABAQUS allows for a frequency domain evaluation of the response for any frequency dependence of the shear modulus and damping coefficient, including the noncausal compromise given by (8). With a frequency domain calculation of the response, one can directly compute the kinematic response function  $I(\omega)$  using equation (5).

### *Kinematic Response Functions*

Figure 5 (left) plots the kinematic response functions along the transverse direction (top) and longitudinal direction (bottom) of the north embankment of the Meloland Road Overcrossing computed with converged values of  $G = 2.0 \text{ MPa}$  and  $\eta = 0.52$ . Figure 5 (right) plots the corresponding kinematic response functions of the west embankment of the Painter Street Bridge for converged value  $G = 8.0 \text{ MPa}$  and  $\eta = 0.5$ . Along the transverse direction, results are obtained with the shear beam approximation (equation (5)) and a 2-D and 3-D finite element analysis. Along the longitudinal direction only a 3-D finite element analysis is meaningful. The results shown on Figure 5 (top) indicate that the shear-beam approximation captures most of the transverse response; whereas the responses computed by assuming a tapered or a prismatic geometry might differ appreciably only at higher frequencies of the longitudinal response. In the bottom plots of Figure 5 we included the kinematic response function along the transverse direction obtained with the shear-wedge approximation in order to show that it can capture most of the amplification generated due to a longitudinal excitation. This comparison is presented in order to validate the use of a single amplification function which can be easily derived from the shear-wedge model and can be applied for both transverse and longitudinal shaking.

### *Validation of Method — Crest Response*

The kinematic response functions shown in Figure 5 can be used to compute the displacement time history at the crest of the embankment

$$u^c(t) = \frac{1}{2\pi} \int_{-\infty}^{\infty} I(\omega) u^b(\omega) e^{i\omega t} d\omega \quad (14)$$

where  $u^b(\omega)$  is the Fourier transform of the base motion. In this study the base motion of the wedge was taken equal to the free-field record.

The validity of the equivalent linear approach expressed with equation (14) is established with motions recorded on the crests of bridge embankments that have been instrumented and subjected to strong shaking. In this study we use records from the Meloland Road Overcrossing and the Painter Street Bridge.

The Meloland Road Overcrossing, located near El Centro in southern California, is a concrete box-girder, two-span bridge with monolithic abutments and a single central column that was designed in 1968. The structure has two spans, each being 104 ft (31.7 m) long and 34 ft (10.36 m) wide. The single-column pier at the center of the bridge is approximately 20 ft (6.1 m) high and is supported by a pile group consisting 25 ( $5 \times 5$ ) driven concrete friction piles. The bridge has monolithic abutments supported by 7 concrete piles driven into stiff clay embankments overlaying native alluvium. The superstructure, abutments, embankments, and free field were instrumented with 26 strong-motion accelerometers (Werner et al. 1987). Figure 6 shows the elevation and plan views of the Meloland Road Overcrossing together with the location of the accelerometers. The bridge was strongly shaken by the October 15, 1979, Imperial Valley earthquake ( $M_L = 6.4$ ) with a peak transverse acceleration of 0.51g recorded on the bridge deck. Figure 7 (left) shows the free-field motions recorded with channels 24 (EW), 15 (NS) and 14 (UP), while Figure 7 (center and right) shows the motions recorded on the north and south embankment respectively.

Figure 8 (left column) plots the transverse crest response of the Meloland Road embankment when computed with equation (14) in which  $I(\omega)$  is given by (5); whereas in the center and right columns, the values of  $I(\omega)$  were computed with a 2-D and 3-D finite element analysis. In the 3-D finite element analysis the 4.4% approach slope of the MRO-embankment was used. The converged values of shear modulus and damping coefficient by the shear-wedge solution are  $G = 2.2MPa$  and  $\eta = 0.52$  that correspond to an average macroscopic strain  $\hat{\gamma} = 5.2 \times 10^{-3}$ . These values are close to the values offered by the 3-D finite element analysis. The final values of the shear modulus and the damping coefficient used in comparison are  $G = 2.0MPa$  and  $\eta = 0.52$ . The relative difference,  $\delta$ , between the maximum values of a computed and recorded response quantity, say  $v$ , is expressed as

$$\delta = 2 \frac{|v^R|_{max} - |v^C|_{max}}{|v^R|_{max} + |v^C|_{max}} \quad (15)$$

where  $|v^R|_{max}$  and  $|v^C|_{max}$  are the maximum recorded and computed response quantities.

Figure 9 plots the longitudinal response of the Meloland Road embankment computed with equation (14) in which  $I(\omega)$  is the corresponding kinematic response function under longitudinal vibrations, shown on the bottom-left of Figure 5. The left column plots the longitudinal response computed with (14) in which  $I(\omega)$  is the kinematic response function obtained with the shear-wedge model in the transverse direction. The center column plots the longitudinal response computed with (14) in which  $I(\omega)$  is the kinematic response function obtained with the prismatic geometry, while the right column plots the longitudinal response computed with  $I(\omega)$  obtained with the tapered geometry.

The foregoing study shows that an equivalent linear analysis yields results on the crest response of a non-skewed embankment that are in satisfactory agreement with the recorded motions ( $4\% \leq \delta \leq 50\%$ ). Furthermore, the 1-D shear-beam approximation offers a realistic estimate for the transverse response of a mildly inclined embankment provided that the equivalent linear properties of the soil material are evaluated at realistic strains. Interestingly, the shear-beam approximation also provides an acceptable prediction of the longitudinal response ( $2\% \leq \delta \leq 67\%$ ). Our study proceeds with the validation of our method against the motions recorded on the skew embankments of the Painter Street Bridge.

The Painter Street Bridge, located near Rio Dell in northern California is a continuous, two-span, cast-in-place, prestressed post-tensioned, concrete, box-girder bridge that was instrumented in 1977 by the California Division of Mines and Geology. Several earthquakes from 1980 to 1987, ranging in magnitude from  $4.4M_L$  to  $6.9M_L$ , have produced significant accelerograms, the peak values of which are summarized by Maroney et al. (1990). The largest peak acceleration of 0.59g was near the center of the bridge deck during a small ( $M_L = 4.4$ ) nearby earthquake.

Maroney et al. (1990) used these records in conjunction with a number of finite element and lumped parameter (stick) models of the entire bridge. However, none of these models accounted for soil-foundation-superstructure interaction. At each abutment, soil-wall interaction was modeled using a single real-valued transverse spring, the stiffness of which was back-calculated from the interpreted small-amplitude fundamental natural period,  $T \approx 0.3s$ , in lateral vibration.

On April 25, 1992, the bridge was severely shaken by the Petrolia earthquake ( $M_L = 7.1$ , distance to the fault  $R = 18km$ ) with a peak transverse acceleration of 0.92g recorded on the bridge deck. Figure 10 shows the elevation and plan views of the Painter Street Bridge together

with the location of accelerometers. Motions were recorded in all accelerographs shown. Figure 11 (left) shows the free-field motions recorded with channel 14 (NS), 12 (EW) and 13 (UP), while Figure 11 (center and right) shows the motions recorded on the west and east embankment respectively.

Before construction, a geotechnical exploration at the locations of the piers was conducted. Using standard penetration test (SPT) measurements from the ground surface down to a depth of about 10 m, moderately stiff/dense soil layers were identified, which consisted of clayey sand, sandy silt, and gravelly sand. SPT blowcounts varied from 8 near the surface to 34 at 10 m depth. The underlying stratum was a very dense gravelly and silty sand, where blowcounts exceeded 100 blows/ft.

In a geophysical exploration by Heuze and Swift (1991) six so-called seismic refraction surveys were reported, along from lines parallel to the highway. Four different idealized soil profiles have emerged as shown in Figure 12. Evidently, the differences in the S-wave velocities and shear moduli among these profiles are substantial, given that they are 20-30 m apart from each other. For instance, the resulting low-strain shear modulus from the data along line 2 is 1.5 times the value of that resulting from the data along line 1. It is quite possible that some of these differences merely reflected inadequacies (general and specific) of the seismic refraction technique. The soil properties used for the dynamic analysis of embankments is taken as a set of uniform values, i.e.,  $\rho_s = 1.6Mg/m^3$ ,  $V_s = 190 m/s$ , and  $\nu = 0.4$  for both west and east embankments. The small-strain shear modulus is  $G_{max} = \rho_s V_s^2 = 58MPa$ .

Figure 13 (left column) plots the transverse crest response of the west embankment at Painter Street Bridge when computed with equation (14) in which  $I(\omega)$  is given by (5). In the center and right columns, the values of  $I(\omega)$  used to compute the crest response were evaluated with 2-D and 3-D finite element analysis. In the 3-D finite element analysis the 5% approach slope of the Painter Street Bridge embankment is used. The converged values of the shear modulus and damping coefficient by the shear-wedge solution are  $G = 7.8MPa$  and  $\eta = 0.50$  that correspond to an average macroscopic strain  $\hat{\gamma} = 4.2 \times 10^{-3}$ . These values are close to the converged values offered by 3-D finite element analysis. The final values of the shear modulus and damping coefficient used in comparison are  $G = 8.0MPa$  and  $\eta = 0.50$ . Again, it is observed that the shear-beam approximation gives an acceptable estimate ( $1\% \leq \delta \leq 12\%$ ) of the response provided that the equivalent linear soil properties are evaluated at a realistic strain level.

Figure 14 plots the longitudinal response of the west embankment of the Painter Street Bridge. The left column plots the computed longitudinal response using the kinematic response function,  $I(\omega)$ , obtained with shear-beam approximation in the transverse direction. The center column plots the computed response when the geometry of the embankment is assumed to be prismatic (zero approaching slope); whereas the right column plots the computed response when the tapered geometry is considered with a slope  $i = 5\%$ . The formulation that accounts for the tapered geometry of the embankment offers better predictions of the relative velocity and displacement histories than the formulation with prismatic geometry. At the same time, the shear-beam approximation gives equally good prediction of longitudinal response ( $\delta \leq 32\%$ ), compared to 3-D finite element analysis that accounts for the tapered geometry of the embankments.

The convincing results offered by the shear-beam approximation shown in both the Meloland Road Overcrossing and Painter Street Bridge cases indicate that the shear-beam approximation, despite its simplicity, is a dependable procedure for estimating the transverse and longitudinal response of bridge embankments.

#### *Summary of Procedure to Compute the Kinematic Response Functions of Embankments*

1. Evaluate the transverse kinematic response function with equation (5) by assuming an initial value of shear modulus,  $G(\gamma)$ , with  $k = \omega\sqrt{\rho/G(\gamma)}$ ;
2. Compute the crest displacement response,  $u_x^c$ , with equation (14);
3. Evaluate the averaged strain,  $\hat{\gamma} = \frac{2}{3}(u_{x,max}^c/H)$ , and the associated shear modulus,  $G(\gamma)$ , and damping coefficient,  $\eta(\gamma)$ , from Figure 2.
4. Repeat steps 1 to 3 until  $\hat{\gamma} = \frac{2}{3}(u_{x,max}^c/H)$  converges.

When a time history is not available, one can assume a realistic value of a soil strain (say  $0.0005 < \gamma < 0.005$ ) and find out the correspondent shear modulus,  $G(\gamma)$  and damping coefficient,  $\eta(\gamma)$ .

## **DYNAMIC STIFFNESSES**

### *Past Studies on Abutment Stiffnesses*

The need to account for the flexibility of abutments when subjected to the inertia forces of the deck has been recognized by several researchers who approached this problem in various ways. Maragakis (1985) proposed a Winkler foundation model to approximate the reaction of soil

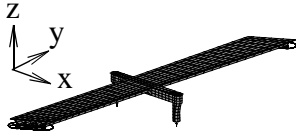
embankments on bridge abutments supported on spread footings. The spring values of the Winkler model were derived using soil mechanics concepts. Recently, his approach was extended by Siddharthan et al. (1993, 1997), who derived simple expressions for the values of the secant stiffnesses of abutments along the longitudinal, vertical, and transverse directions. Their simple expressions were found to agree with the experimental data from large-scale experiments conducted by Romstad et al. (1995). Crouse et al. (1987) conducted small-amplitude harmonic tests on the Horsethief Road Bridge and subsequently back-figured the values of distributed springs that approximated the interaction between abutment wall and backfill soil. The spring value that resulted from such small-amplitude tests is at the high end and is not practical for design under intense earthquake loading, since abutment stiffnesses are amplitude dependent. Motivated from the need to obtain more realistic values of abutment stiffnesses under strong ground motions, Goel and Chopra (1997) back-figured the force-displacement loops at the abutments of the Painter Street Bridge by investigating its recorded response under several earthquakes. Other studies have been conducted by Werner et al. (1994) and McCallen and Romstad (1994), who concluded that abutment stiffnesses are much lower and modal damping ratios much higher than previously deduced from low-amplitude tests. A large-scale experimental program was conducted by Romstad et al. (1995) to evaluate the stiffnesses and strengths of abutments. Table 1 summarizes various values of stiffnesses of bridge abutments that have been reported in the literature or that have been calculated with proposed methods. Table 1 includes the values used by Caltrans and the values that one computes using the closed-form expressions derived by Wilson and Tan (1990a). All stiffness values have been normalized by the width of the embankment, so the resulting unit is  $[\text{Force}]/[\text{Length}]^2$ . The large discrepancies shown in Table 1 motivated the need for an integrated procedure in estimating the stiffnesses of abutments, which depend strongly on the level of strains that develop in the approach embankments. For instance under strong ground shaking the Caltrans values offered by method A are divided in practice by four (Delis 1999).

### *The Shear Beam Approximation*

The Wilson and Tan expressions, given by equations (16) and (17) of this paper, were derived by integrating the incremental displacements of a slice of unit width of the wedge due to a distributed load at the crest.

$$\hat{k}_x(0) = \frac{2G}{S \ln\left(1 + \frac{2H}{SB_c}\right)} \quad (16)$$

**Table 1: Comparisons of estimated abutment/embankment stiffnesses**

		Meloland Road Overcrossing $H = 7.92 \text{ m}$ , $B_c = 10.36 \text{ m}$ , $S = 1/2$ , $L_c = 4.5 \text{ m}$ , $\rho = 1.6 \text{ Mg/m}^3$ , $G_{max} = 19 \text{ MPa}$ , $G = 2 \text{ MPa}$ , $\eta = 0.52$			Painter Street Bridge $H = 9.6 \text{ m}$ , $B_c = 15.24 \text{ m}$ , $S = 1/2$ , $L_c = 6.0 \text{ m}$ , $\rho = 1.6 \text{ Mg/m}^3$ , $G_{max} = 58 \text{ MPa}$ , $G = 8 \text{ MPa}$ , $\eta = 0.50$			Large Scale Field Test $H = 2.06 \text{ m}$ , $B_c = 4.72 \text{ m}$ , $S = 1/2$ , $L_c = 1.5 \text{ m}$ , $\rho = 1.8 \text{ Mg/m}^3$ , $G_{max} = 72 \text{ MPa}$			
		Stiffnesses ( $\text{MN/m}^2$ )			$K_x/B_c$	$K_y/B_c$	$K_z/B_c$	$K_x/B_c$	$K_y/B_c$	$K_z/B_c$	$K_x/B_c$
1	Douglas et al. 1991	8.8	8.8	25.4	/	/	/	/	/	/	/
2	Maroney et al. 1993	/	/	/	/	/	/	2.6~7.4	3.7~11.1	/	/
3	McCallen & Romstad 1994	/	/	/	56.0	53.0	/	/	/	/	/
4	Werner 1994	10.3	/	/	/	/	/	/	/	/	/
5	Goel & Chopra 1997	/	/	/	9.6~14.0	9.6~46.9	/	/	/	/	/
6	Price and Eberhard 1998	/	/	/	4.7	/	/	/	/	/	/
7	Caltrans: Method A	58.6	57.5	/	53.2	57.5	/	44.6	57.5	/	/
8	Caltrans: Method B	7.4	/	/	6.9	/	/	2.6~3.4	/	/	/
9	Wilson 1988	12.1	12.1	16.1	24.6	24.9	52.5	/	/	/	/
10	Wilson & Tan 1990a	3.3	/	9.2	13.2	/	37	/	/	/	/
11	Siddharthan et al 1997	10~48	0.3~1.5	12~54	27~126	0.7~3.4	21.6~101.3	1.5~6.8	0.1~0.4	1.1~4.9	/
12	FEM 3D	2~3	2~3.1	7.5	9~14	9~13.8	38.2	/	/	/	/
13	Proposed Simple Procedure	2	2	/	10	10	/	/	/	/	/
Note	1. Values are identified from records, pile foundation stiffnesses are included. 2. Experimental results, pile foundation stiffnesses are included. 3. Per Caltrans procedure A, pile foundation stiffnesses are not included. 4. Best identified value, including pile foundation stiffnesses. 5. Back-figured values, including pile foundation stiffnesses. 6. Pile foundation stiffnesses are not included. 7. Use $(200 \text{ kips/in/ft}) \cdot (2/3 \text{ wingwall length}) \cdot 4/3$ in transverse direction and $(200 \text{ kips/in/ft}) \cdot (0.5 \cdot \text{embankment width})$ in longitudinal direction. 8. Use $7.7 \text{ ksf} \cdot (\text{effective wingwall area}) / 0.2 \text{ ft}$ . 9. Use converged shear modulus and damping coefficient without including pile foundation stiffnesses. 10. Same as 9, use eq. (16) and (17) multiplied by the wingwall length. 11. Unable to reproduce the results in longitudinal direction with the formulations presented in their paper. Pile foundation stiffnesses are not included. 12. Same as 9. 13. Use unit-width shear-wedge solution multiplied by critical length, $L_c = 0.7 \sqrt{SB_c H}$ . Pile foundation stiffnesses are not included.										



$$\hat{k}_z(0) = \frac{2E}{S \ln\left(1 + \frac{2H}{SB_c}\right)} \quad (17)$$

where  $G$  is the converged value of the shear modulus that is concluded from the kinematic response analysis and  $E = 2(1 + \nu)G$  is the associated Young's modulus. To translate the results of equation (16) to the values of the static stiffness of the entire embankment one has to multiply  $\hat{k}_x(0)$  with some critical length,  $L_c$ , along the longitudinal direction of the embankment. One approximation is to use the length of the wingwall. A more rational value for length,  $L_c$ , is proposed below. The expressions given by (16) and (17) assume that the ground beneath the embankment is rigid and does not undergo any deformation; whereas its geometry is symmetric, having the same slope on each side. For the general case of a nonsymmetric cross section (see Figure 1(top)), the transverse displacement at the top of unit-width wedge due to a distributed load,  $p_x$ , at the crest is given by

$$u_x = \int_{z_0}^{z_0+H} \gamma dz = \int_{z_0}^{z_0+H} \frac{p_x}{G} \cdot \frac{z_0}{zB_c} dz = \frac{p_x z_0}{GB_c} \ln\left(\frac{z_0+H}{z_0}\right). \quad (18)$$

and the transverse static stiffness of the unit-width wedge is thus given by

$$\hat{k}_x(0) = \frac{p_x}{u_x} = \frac{GB_c}{z_0 \ln\left(\frac{z_0+H}{z_0}\right)}. \quad (19)$$

Similarly, the vertical static stiffness due to a distributed load at the crest is given by

$$\hat{k}_z(0) = \frac{p_z}{u_z} = \frac{EB_c}{z_0 \ln\left(\frac{z_0+H}{z_0}\right)} \quad (20)$$

For the case of a symmetric embankment equations (19) and (20) reduce to equations (16) and (17), since  $z_0 = \frac{1}{2}B_c S$ .

The static solutions derived by Wilson and Tan (1990a) for the case of a symmetric embankment or the more general expressions offered by equations (19) can be extended for harmonic distributed loads at the crest. With reference to Figure 15 (top), considering a distributed harmonic loading,  $p_x e^{i\omega t}$ , that creates horizontal crest displacement,  $u_x e^{i(\omega t - \phi)}$ , dynamic equilibrium of a section,  $dz$ , of the wedge gives

$$\frac{\partial}{\partial z} Q(z, t) = \rho A(z) \frac{\partial^2}{\partial t^2} u_x(z, t) \quad (21)$$

where  $Q(z, t)$  is the time-dependent shear force at depth  $z$ . Using that

$$\frac{Q(z, t)}{A(z)} = \tau(z) = G\gamma(z) = G \frac{\partial}{\partial z} u_x(z, t) \quad (22)$$

equation (21) becomes

$$\frac{\partial^2}{\partial z^2} u_x(z, t) + \frac{1}{z} \frac{\partial}{\partial z} u_x(z, t) = \frac{1}{V_s^2} \frac{\partial^2}{\partial t^2} u_x(z, t) \quad (23)$$

The solution of equation (23) is offered below for limiting cases where (a) the supporting soil is rigid and does not accommodate any deformation and (b) the supporting soil is deformable to the extent that the embankment wedge can be extended into the halfspace over a large depth. The boundary conditions for case (a) are that the displacements at depth  $z = z_0 + H$  are zero, while the shear force at the crest is equal to the external load, i.e.,  $Q(z_0, t) = p_x e^{i\omega t}$ . The boundary condition for the case (b) is that there are no incoming waves (Sommerfeld radiation condition — see Wolf (1994) among others), while the shear force  $Q(z_0, t) = p_x e^{i\omega t}$ . With these boundary conditions the solution of (23) for case (a) is

$$u_x(z, t) = \frac{1}{GB_c k} \cdot \frac{Y_0[k(z_0 + H)]J_0(kz) - J_0[k(z_0 + H)]Y_0(kz)}{J_1(kz_0)Y_0[k(z_0 + H)] - J_0[k(z_0 + H)]Y_1(kz_0)} p_x e^{i\omega t} \quad (\text{rigid supporting soil}) \quad (24)$$

and for case (b) is

$$u_x(z, t) = \frac{1}{GB_c k} \cdot \frac{H_0^{(2)}(kz)}{H_1^{(2)}(kz_0)} p_x e^{i\omega t} \quad (\text{infinitely tall wedge}) \quad (25)$$

At the crest of the embankment

$$p_x(z_0, t) = \hat{k}_x(\omega) u_x(z_0, t) \quad (26)$$

and for each of these cases (a) and (b) equation (26) gives

$$\hat{k}_x(\omega) = G(1 + i\eta) B_c k \cdot \frac{J_1(kz_0)Y_0[k(z_0 + H)] - J_0[k(z_0 + H)]Y_1(kz_0)}{Y_0[k(z_0 + H)]J_0(kz_0) - J_0[k(z_0 + H)]Y_0(kz_0)} \quad (\text{rigid supporting soil}) \quad (27)$$

and

$$\hat{k}_x(\omega) = G(1+i\eta)B_c k \frac{H_1^{(2)}(kz_0)}{H_0^{(2)}(kz_0)} \text{ (infinitely tall wedge)} \quad (28)$$

Figures 16 and 17 plot the real and imaginary parts of the dynamic stiffnesses given by equation (27) (left, rigid support) and equation (28) (right, infinitely tall wedge). In Figure 16 the material and geometrical properties,  $G = 2MPa$ ,  $\eta = 0.52$ ,  $z_0 = 2.59m$ ,  $H = 7.92m$ , and  $B_c = 10.36m$  of the Meloland Road Overcrossing are used; whereas in Figure 17 the material and geometrical properties,  $G = 8MPa$ ,  $\eta = 0.5$ ,  $z_0 = 3.81m$ ,  $H = 9.6m$ , and  $B_c = 15.24m$  of the Painter Street Bridge are used.

### *Finite Element Analysis*

The ability of the shear-wedge model to approximate the transverse dynamic stiffness of an approach embankment is examined in this section by conducting finite element analysis on a unit-width wedge. Figures 16 and 17 show finite element solutions for the transverse dynamic stiffness of the unit-width wedge. In the case of the infinitely tall wedge (flexible support), the supporting soil is represented by the 2-D infinite element with the soil properties same as that of the embankments. The solution is computed by imposing a transverse oscillating load,  $p_x e^{i\omega t}$  at the crest of the wedge and computing the resulting displacement,  $u_x e^{i(\omega t - \phi)}$ . By definition, the dynamic stiffness is

$$k_x(\omega) = k_{1x}(\omega) + ik_{2x}(\omega) = \frac{P_x e^{i\omega t}}{u_x e^{i(\omega t - \phi)}} = \frac{P_x}{u_x} e^{i\phi} \quad (29)$$

The dashed lines in Figures 16 and 17 are the results from a 2-D finite element analysis; whereas the chain line in these figures is the finite element solution that is obtained by restraining the vertical degree of freedom. The real part of solutions given by (27) at static limit agrees with the solution of Wilson and Tan (1990a), while the solutions from 2-D finite element analysis follow the similar trend with the analytical solution but with slightly lower values. The practical spring values shown in the top left of Figures 16 and 17 are frequency independent springs that are recommended in this study to approximate the low frequency values of storage stiffness. Similarly the practical dashpot values is the slope of a line that capture the average slope of the loss stiffness shown in bottom left plots. Because of the unit-width of the wedge, the units of equation (29) are  $[Force]/[length]^2$ . To translate the results of equations (27) to (29) to values that reflect the dynamic stiffness of the entire embankment, one has to multiply the computed values with a

critical length  $L_c$ . Wilson and Tan (1990b) proposed to use as critical length the length of the wing wall. Herein a 3-D finite element study is conducted to further investigate this issue.

Figure 18 shows an isoparametric schematic of an approach embankment subjected to transverse (top) and longitudinal (bottom) oscillatory loads,  $p_x e^{i\omega t}$  and  $p_y e^{i\omega t}$ . Under harmonic loading along direction  $j$  ( $j \in (x, y)$ ), the resulting displacement is harmonic,  $u_j e^{i(\omega t - \phi)}$ , where  $\phi$  is the phase difference between displacement and force. Along any direction,  $j$ , the dynamic stiffness is defined as

$$k_j(\omega) = k_{1j}(\omega) + ik_{2j}(\omega) = \frac{p_j e^{i\omega t}}{u_j e^{i(\omega t - \phi)}} = \frac{p_j}{u_j} e^{i\phi} \quad (30)$$

The ratio  $p_j/u_j$  is a real and frequency-dependent quantity known as the total distributed stiffness,  $k_{0j} = p_j/u_j$ , whereas  $k_{1j}(\omega) = p_j/u_j \cos(\phi)$  is the distributed storage stiffness and  $k_{2j}(\omega) = p_j/u_j \sin(\phi)$  is the distributed loss stiffness.

The computer software ABAQUS (1997) is used to conduct the forced-vibration dynamic analysis of bridge embankments under the loadings shown in Figure 18. Figure 19 plots the computed real part (storage stiffness) and the imaginary part (loss stiffness) of the Meloland Road Overcrossing embankments under transverse, longitudinal, and vertical distributed loadings. The values of  $G$  and  $\eta$  of embankment soil used in the elastic analysis are the converged values of  $G = 2.0MPa$  and  $\eta = 0.52$  that were determined from the forced vibration of the embankment under base shaking. The shear modulus of supporting soil underneath the embankment is taken as  $G_s/G = \infty, 10$  and  $1$ , in order to examine the effect of the flexibility of the supporting soil. Figure 19 indicates that the effect of the stiffness of the supporting soil is marginal in both the transverse and longitudinal directions; therefore the solution of the embankment sitting on a rigid support can be used with confidence. Similarly, Figure 20 plots the computed real and imaginary parts of Painter Street Bridge embankments under transverse, longitudinal, and vertical loadings. The values of  $G$  and  $\eta$  of embankment soil used in the elastic analysis are the converged values  $G = 8.0MPa$  and  $\eta = 0.5$ , also determined from the forced vibration of the embankment under the corresponding base shaking. The slope of the loss stiffness gives the dashpot values. The spring and dashpot values can be extracted by multiplying the values shown in figures 19 and 20 with the width of the embankment,  $B_c$ .

### Estimation of Critical Length $L_c$

While 3-D finite element calculations are necessary in this study to establish the dynamic stiffnesses of approach embankments, our study proceeds with the development of a practical procedure that allows for the estimation of the dynamic stiffnesses of the embankments by using the stiffness and damping values of a unit-width shear wedge and a critical length,  $L_c$ . The transverse mechanical behavior of an infinitely long embankment due to a concentrated load at one end is idealized with a series of unit-width wedges interacting in shear with one another. Figure 21 shows a long embankment subjected to a transverse load,  $P_x$ , at its front end and a slice of the embankment with width,  $dy$ . Within the context of 1-D analysis the equilibrium of the section along the transverse direction gives

$$Q(y) + \frac{d}{dy}Q(y)dy - Q(y) - \hat{k}_x u_x(y)dy = 0 \quad (31)$$

which gives

$$\frac{d}{dy}Q(y) - \hat{k}_x u_x(y) = 0 \quad (32)$$

In equations (31) and (32),  $u_x(y)$  is the transverse displacement of some reference point on the section,  $\hat{k}_x$  is the static stiffness of the unit-width wedge given by (16) or (19), and  $Q(y)$  is the shear force on the face of the section of the slice that is approximated with

$$Q(y) = AG \frac{d}{dy} u_x(y) \quad (33)$$

substitution of (19) and (33) into (32) gives

$$AG \frac{d^2}{dy^2} u_x(y) - \frac{GB_c}{z_0 \ln\left(1 + \frac{H}{z_0}\right)} u_x(y) = 0 \quad (34)$$

Equation (34) reduces to

$$\frac{d^2}{dy^2} u_x(y) - \lambda^2 u_x(y) = 0 \quad (35)$$

where

$$\lambda = \sqrt{\frac{B_c}{z_0 A \ln(1 + H/z_0)}} \quad (36)$$

Using that at large values of  $y$  the displacement,  $u_x(y)$ , vanishes, the solution of (35) becomes

$$u_x(y) = Ce^{-\lambda y} \quad (37)$$

where  $C$  is an integration constant that is determined from the boundary conditions. The force at the origin is given by (33) after setting  $y = 0$

$$P = -Q(0) = -AGC(-\lambda) \quad (38)$$

from which

$$C = \frac{P}{AG\lambda} \quad (39)$$

Substitution of (39) to (37) gives the approximate expression for the displacement distribution

$$u_x(y) = \frac{P}{AG\lambda} e^{-\lambda y} \quad (40)$$

which when evaluated at  $y = 0$  gives an estimate of the dynamic stiffness of the embankment

$$K_x = \frac{P}{u_x(0)} = AG\lambda = G \sqrt{\frac{B_c A}{z_0 \ln(1 + H/z_0)}} \quad (41)$$

For the case of a symmetric embankment,  $z_0 = B_c S/2$ , equation (41) reduces to

$$K_x = G \sqrt{\frac{2A}{S \ln\left(1 + \frac{2H}{SB_c}\right)}} \quad (42)$$

Equation (42) is the extension of the solution for the static stiffness of the unit-width wedge that was derived by Wilson and Tan (1990a). Equation (42) in association with (16) yield an expression for the critical length,  $L_c$ , that is needed to multiply the static stiffness of the unit-width wedge to estimate the transverse stiffness of the embankment. Wilson and Tan (1990b) have assumed that  $L_c$  should be approximately the length of the wing wall. In this study we conclude that

$$K_x = G \sqrt{\frac{2A}{S \ln\left(1 + \frac{2H}{SB_c}\right)}} = L_c \hat{k}_x = L_c \frac{2G}{S \ln\left(1 + \frac{2H}{SB_c}\right)} \quad (43)$$

which gives

$$L_c = \frac{K_x}{k_x} = \frac{\sqrt{2}}{2} \cdot \sqrt{AS \ln\left(1 + \frac{2H}{SB_c}\right)} \quad (44)$$

Equation (44) indicates that the critical length is independent of the shear modulus,  $G$ , and is proportional to the square root of the area,  $A$ , and the slope of the embankment,  $S$ .

Equation (44) was derived by relating the expression of the static stiffness of the unit-width wedge to the approximate closed-form expression of the static stiffness of the embankment given by (42). If instead of the values provided by (42) one uses the more exact finite element results, the foregoing analysis suggests that a good candidate expression for the critical length,  $L_c$ , is

$$L_c = \frac{K_x}{k_x} = \alpha \sqrt{SB_c H} \quad (45)$$

where the quantity  $\sqrt{SB_c H}$  accommodates the physics that emerges from  $\sqrt{AS \ln(1 + 2H/(SB_c))}$  and  $\alpha$  is a dimensionless coefficient that is expected to be nearly independent of the geometry. Figure 22 plots the coefficient,  $\alpha = K_x / (k_x \sqrt{SB_c H})$  for various embankment geometries. Figure 22 indicates that  $\alpha \approx 0.7$  is indeed nearly independent of geometry for the embankment configurations of interest. Therefore, it is suggested that the critical length,  $L_c$ , is given by

$$L_c \approx 0.7 \sqrt{SB_c H} \quad (46)$$

The concept of the critical length,  $L_c$ , which relates the stiffness of the unit-width wedge to the stiffness of the embankment, is extended for the case of damping. Accordingly, it is proposed that the dynamic stiffness of the embankment is given by

$$\mathcal{K}_x = \hat{k}_x(\omega) \cdot L_c \quad (47)$$

where  $\hat{k}_x(\omega)$  is the dynamic stiffness of the unit-width wedge given by (27) and  $L_c$  is a critical length that is given by (46). The good estimates for the stiffness and dashpot values given by (47) where the critical length is given by (46), is shown in Figure 19 and 20 together with the 3-D finite element solutions.

### *Summary of Procedure to Compute the Spring and Dashpot Values of Bridge Embankments*

1. Compute the dynamic stiffness of the unit-width shear wedge using equation (27). The values of  $G$  and  $\eta$  in this equation are the converged values obtained from the calculation of the kinematic response functions. The Bessel functions appearing in equations (27) can be automatically computed with commercially available software such as MATLAB.

2. Plot the real and imaginary part of equation (27) as a function of frequency,  $f = \frac{\omega}{2\pi}$  ( $k = \text{wave number} = \omega/[V_s(1 + i\eta)]$  and  $V_s = \sqrt{G/\rho}$ ).
3. Select practical spring and dashpot values by passing a horizontal line through the graph of the real part and an inclined line through the graph of the imaginary part at locations that capture with satisfaction the low frequency behavior (see Figures 16 and 17). If only spring values are of interest, steps 1 to 3 can be avoided by merely using the Wilson and Tan (1990a) expression (equation (16)) or the more general expressions offered by equation (19). Steps 1 to 3 are primarily needed to estimate the dashpot values.
4. Compute the transverse spring and dashpot values of the embankment by multiplying the values indicated by the lines identified in step 3 with the critical length,  $L_c \approx 0.7\sqrt{SB_cH}$ .
5. For the longitudinal spring and dashpot values to represent the approach embankment, use the spring and dashpot values computed in step 4 .

## CONCLUSIONS

Recognizing that soil-structure interaction affects appreciably the earthquake response of highway overcrossings, the kinematic response functions and dynamic stiffnesses of their approach embankment were revisited and it was concluded that:

- During strong shaking soil strains in bridge embankment can be as high as  $\gamma \approx 5 \times 10^{-3}$  or even more, resulting in equivalent linear shear modulus,  $G \approx G_{max}/10$ , and damping coefficient,  $\eta \approx 0.5$ .
- Typical approach embankments even when strained at the above indicated levels tend to amplify substantially the free field motions (two to three times).
- The dynamic stiffnesses of embankments, although in theory are frequency dependent, they can be approximated in practice with frequency independent “springs” and “dashpots”.
- The unit-width shear-wedge model can be extended to a two-dimensional model that yields estimates of the transverse static stiffness of approach embankments when loaded at one end that are in agreement with 3D finite element analysis. The formulation reveals a sound closed form expression for the critical length,  $L_c$ , that is the ratio of the transverse static stiffness of an approach embankment to the transverse static stiffness of a unit-width wedge.



- The simple expression for the critical length,  $L_c \approx 0.7 \sqrt{SB_c H}$  allows for a realistic estimation of the dynamic stiffness of the approach embankment from the dynamic stiffness of a unit-width shear-wedge.

### ACKNOWLEDGEMENTS

Partial financial support for this study was provided by the National Science Foundation under Grant CMS-9696241. The valuable input and comments of Dr. Tim Delis are appreciated.

### REFERENCES

1. AASHTO-83 (1988), *Guide Specifications for Seismic Design of Highway Bridges*, American Association of State Highway and Transportation Officials, Washington, D. C.
2. ABAQUS (1997), Hibbitt, Karlsson & Sorensen, Inc.
3. Abramowitz, M. and Stegun, I. A. (1970), *Handbook of Mathematical Functions With Formulas, Graphs, and Mathematical Tables*, Dover Publications, Inc., New York, NY.
4. CALTRANS (1989), *Bridge Design Aids 14-1*, California Department of Transportation, Sacramento, CA.
5. Caughey, T. K. (1962), "Vibrations of dynamic systems with linear hysteretic damping (linear theory)", *Proc. 4th U. S. Natl. Congr. Appl. Mech.*, ASME, New York, NY, pp. 87-97.
6. Crandall, S. H. (1963), "Dynamic response of systems with structural damping", *Air, Space and Instruments, Draper Anniversary*, S. Lees ed., McGraw Hill, New York, NY, pp. 183-193.
7. Crandall, S. H. (1970), "The role of damping in vibration theory", *Journal of Sound and Vibration*, Vol. 11, No. 1, pp. 3-18.
8. Crouse, C. B., Hushmand, B., and Martin, G. R. (1987), "Dynamic soil-structure interaction of single-span bridge", *Earthquake Engineering and Soil Dynamics*, Vol. 15, pp. 711-729.
9. Dakoulas, P., and Gazetas, G. (1985), "A class of inhomogeneous shear models for seismic response of dams and embankments", *Soil Dynamics and Earthquake Engineering*, Vol. 4, No. 4, pp. 166-182.
10. Delis, E.A. (1999), Personal communications.
11. Delis, E.A., Malla, R. B., Madani, M. and Thompson, K. J. (1996), "Energy dissipation devices in bridges using hydraulic dampers", *Proc. Structures Congress XIV*, Chicago, IL, Vol. 2, pp. 1188-1196.

12. Douglas, B. M., Maragakis, E., and Vrontinos, S. (1991), "Parameter identification studies of the Meloland Road Overcrossing", *Proc. Pacific Conference on Earthquake Engineering*, Auckland, New Zealand, Vol. 1, pp. 105-116.
13. FHWA (1995), *Seismic Retrofitting Manual for Highway Bridges*, Publication No. FHWA-RD-94-052, McLeon, VA.
14. Flugge, W. (1975), *Viscoelasticity*, Springer, New York, NY.
15. Gazetas, G. (1987), "Seismic response of earth dams: some recent developments", *Soil Dynamics and Earthquake Engineering*, Vol. 6, No. 1, pp. 2-47.
16. Goel, R. K., and Chopra, A. K. (1997), "Evaluation of bridge abutment capacity and stiffness during earthquakes", *Earthquake Spectra*, Vol. 13, No. 1, pp. 1-23.
17. Hardin, B. O. (1965), "The nature of damping in sand", *Journal of Soil Mechanics & Foundation Engineering*, ASCE, Vol. 91, pp. 63-97.
18. Heuze, F. E., and Swift, R. P. (1991), "Seismic refraction studies at the Painter Street Bridge site, Rio Dell, California", *Rep. UCRL-ID-108595*, Lawrence Livermore National Laboratory, Oak Ridge, TN.
19. Idriss, I. M., Seed, H. B., and Serff, N. (1974), "Seismic response by variable damping finite elements", *Journal of Geotechnical Engineering*, Vol. 100, No. GT1, pp. 1-13.
20. Inaudi, J. A., and Kelly, J. M. (1995), "Linear hysteretic damping model and the Hilbert transform", *Journal of Engineering Mechanics*, ASCE, Vol. 121, NO. 5, pp. 626-632.
21. Iwasaki, T., Tatsuoka, F., and Takagi, Y. (1978), "Shear moduli of sands under cyclic torsional shear loading", *Soils and Foundations*, Vol. 18, No. 1, pp. 39-56.
22. Makris, N. (1997), "Causal Hysteretic Element", *Journal of Engineering Mechanics*, ASCE, Vol. 123, No. 11, pp. 1209-1214.
23. Makris, N., and Zhang, J. (2000), "Time-domain viscoelastic analysis of earth structures", *Earthquake Engineering and Structural Dynamics*, Vol. 29, pp. 745-768.
24. Maragakis, E. A. (1985), "A model for the rigid body motion of skew bridges", *Report No. EERL 85-02*, Caltech, Pasadena, CA.
25. Maragakis, E. A., and Jennings, P. C. (1987), "Analytical models for the rigid body motions of skew bridges", *Earthquake Engineering and Structural Dynamics*, Vol. 15, No. 8, pp. 923-944.

26. Maroney, B., Romstad, K. and Chajes, M. (1990), "Interpretation of Rio Del freeway response during six recorded earthquake events", *Proc. 4th U.S. National Conference on Earthquake Engineering*, Vol. 1, pp. 1007-1016.
27. Maroney, B. A., Romstad, K. M., and Kutter, B. (1993), "Experimental testing of laterally loaded large scale bridge abutments", *Structural Engineering in Natural Hazards Mitigation: Proceedings of Papers Presented at the Structures Congress '93*, ASCE, New York, Vol. 2, pp. 1065-1070.
28. McCallen, D. B., and Romstad, K. M. (1994), "Analysis of a skewed short-span, box-girder overpass", *Earthquake Spectra*, Vol. 10, No. 4, pp. 729-755.
29. Mononobe, H. A. (1936), "Seismic stability of the earth dam", *Proc. 2nd Congress on Large Dams*, Washington D.C., IV.
30. Price, T. E. and Eberhard, M. O. (1998), "Efficient procedure for modeling the transverse seismic response of bridge embankments", *Proc., Sixth U.S. National Conference on Earthquake Engineering*, Earthquake Engineering Research Inst., Oakland, CA.
31. Priestley, M. J. N., Seible, F., and Calvi, G. M. (1996), *Seismic Design and Retrofit of Bridges*, John Wiley, New York, NY.
32. Romstad, K. M., Kutter, B., Maroney, B., Vanderbilt, E., Griggs, M., and Chai, Y. H. (1995), "Experimental measurements of bridge abutment behavior", *Report No. UCD-STR-95-1*, University of California, Davis, CA.
33. Seed, H. B., and Idriss, I. M. (1969), "Influence of soil conditions on ground motions during earthquakes", *Journal of Soil Mechanics and Foundations*, ASCE, Vol. 95, No. SM1, pp. 99-137.
34. Seed, H. B., and Idriss, I. M. (1970), "Soil moduli and damping factors for dynamic response analysis", *Report No. EERC 70-10*, University of California, Berkeley, CA.
35. Siddharthan, R., El-Gamal, M., and Maragakis, E.A. (1993), "Investigation of performance of bridge abutments in seismic regions", *Journal of Structural Engineering*, ASCE, Vol. 120 (4), pp. 1327-1346.
36. Siddharthan, R., El-Gamal, M., and Maragakis, E. A. (1997), "Stiffnesses of abutments on spread footings with cohesionless backfill", *Canadian Geotechnical Journal*, Vol. 34, No. 5, pp. 686-697.

37. Skinner, R. I., Robinson, W. H., and McVerry, G. H. (1993), *An introduction to seismic isolation*, John Wiley & Sons, Chichester, U. K. and New York, NY.
38. Tatsuoka, F., Iwasaki, T., and Takagi, Y. (1978), "Hysteretic damping of sands under cyclic loading and its relation to shear modulus", *Soils and Foundations*, Vol. 18, No. 2, pp.25-40.
39. Vucetic, M., and Dobry, R. (1991), "Effect of soil plasticity on cyclic response", *Journal of Geotechnical Engineering*, ASCE, Vol 117, No. 1, pp. 89-107.
40. Werner, S. D., Beck, J. L., and Levine, M. B. (1987), "Seismic response evaluation of Meloland road overpass using 1979 Imperial valley earthquake records", *Earthquake Engineering and Structural Dynamics*, Vol. 15, pp. 249-274.
41. Werner, S. D. (1994), "Study of Caltrans' seismic evaluation procedure for short bridges", *Proc. 3rd Annual Seismic Research Workshop*, California Department of Transportation, Sacramento, California.
42. Wilson, J.C. (1988), "Stiffness of non-skew monolithic bridge abutments for seismic analysis", *Earthquake Engineering & Structural Dynamics*, Vol. 16, No. 6, pp.867-883.
43. Wilson, J. C., and Tan, B. S. (1990a), "Bridge abutments: formulation of simple model for earthquake response analysis", *Journal of Engineering Mechanics*, Vol. 116, No. 8, pp. 1828-1837.
44. Wilson, J. C., and Tan, B. S. (1990b), "Bridge abutments: accessing their influence on earthquake response of Meloland Road Overpass", *Journal of Engineering Mechanics*, Vol. 116, No. 8, pp. 1838-1856.
45. Wolf, J. P. (1994), *Foundation Vibration Analysis Using Simple Physical Models*, Prentice-Hall, Inglewood Cliffs, NJ.

## FIGURE LEGENDS

Figure 1. Cross section of infinitely long embankment (top); Isoparametric view of approach embankment (center); geometrical and material characteristics of embankments of two instrumented bridges in California(bottom)

Figure 2. Normalized soil shear modulus and damping coefficient ( $\eta = 2\xi$ ) as a function of shear strain

Figure 3. Strain time histories at base, center, and near top of Meloland Road Overcrossing soil embankment computed with Rayleigh damping approximation ( $G = 1.5MPa$ ,  $\eta = 0.56$ ,  $\alpha = 2.1191$ , and  $\beta = 3.7411 \times 10^{-2}$ )

Figure 4. Strain time histories at base, center, and near top of Painter Street Overcrossing soil embankment computed with Rayleigh damping approximation ( $G = 9.4MPa$ ,  $\eta = 0.48$ ,  $\alpha = 3.7324$ , and  $\beta = 1.4897 \times 10^{-2}$ )

Figure 5. Kinematic response functions of Meloland Road Overcrossing embankment (left) and Painter Street Overcrossing embankment (right)

Figure 6. Elevation and plan views of Meloland Road Overcrossing along with locations of accelerometers

Figure 7. Recorded acceleration time histories at free field (left), north embankment (center), and south embankment (right) of Meloland Road Overcrossing during 1979 Imperial Valley earthquake

Figure 8. Transverse crest response of Meloland Road Overcrossing embankment computed with shear-beam approximation (left), two-dimensional finite element method (center), and three-dimensional finite element method (right)

Figure 9. Longitudinal crest response of Meloland Road Overcrossing embankment computed with shear-beam approximation (left), three-dimensional prismatic geometry (center), and three-dimensional tapered geometry (right)

Figure 10. Elevation and plan views of Painter Street Overcrossing along with locations of accelerometers

Figure 11. Recorded acceleration time histories at free field (left), west embankment (center), and east embankment (right) of Painter Street Overcrossing during 1992 Petrolia earthquake

Figure 12. Idealized soil profiles that emerged from refraction surveys (Heuze and Swift 1991)

Figure 13. Transverse crest response of Painter Street Overcrossing embankment computed with shear-beam approximation (left), two-dimensional finite element method (center), and three-dimensional finite element method (right)

Figure 14. Longitudinal crest response of Painter Street Overcrossing embankment computed with shear beam approximation (left), three-dimensional prismatic geometry (center) and three-dimensional tapered geometry (right)

Figure 15. Unit-width finite wedge (top) and infinitely tall wedge (bottom)

Figure 16. Transverse dynamic stiffnesses of shear-wedge model and solution of two-dimensional finite element formulation. Left: finite wedge on rigid support; Right: infinitely tall wedge. Material and geometrical properties are those of Meloland Road Overcrossing ( $G = 2MPa$ ,  $\eta = 0.52$ ,  $z_0 = 2.59m$ ,  $H = 7.92m$ , and  $B_c = 10.36m$ )

Figure 17. Transverse dynamic stiffnesses of shear-wedge model and solution of two-dimensional finite element formulation. Left: finite wedge on rigid support; Right: infinitely tall wedge. Material and geometrical properties are those of Painter Street Overcrossing ( $G = 8MPa$ ,  $\eta = 0.5$ ,  $z_0 = 3.81m$ ,  $H = 9.6m$ , and  $B_c = 15.24m$ )

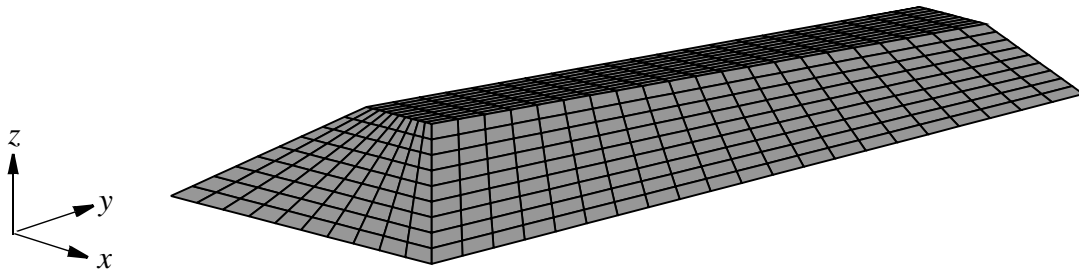
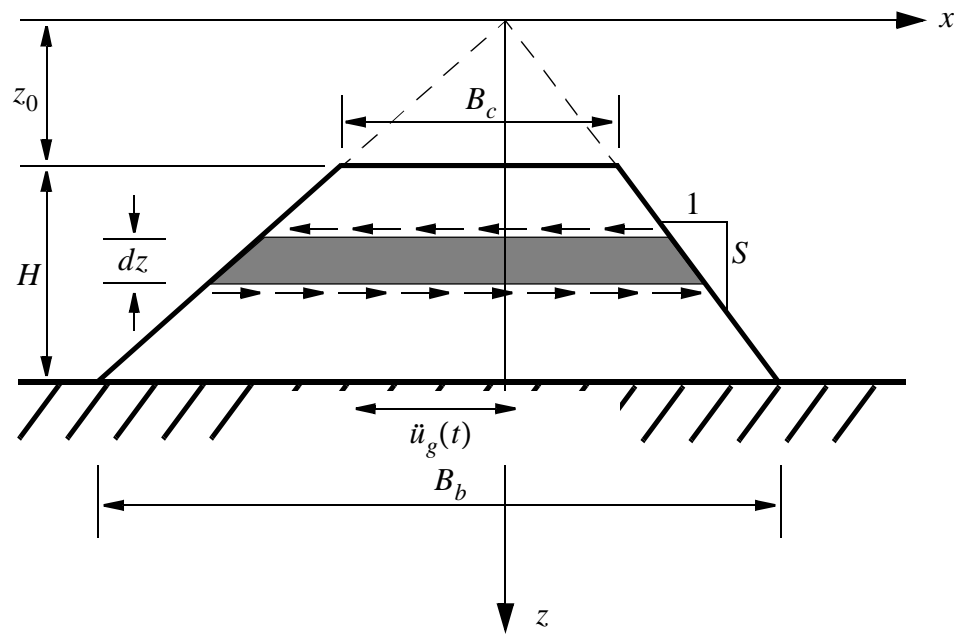
Figure 18. Transverse and longitudinal loading imposed to obtain dynamic stiffness of approach embankment with material properties,  $G$  and  $\eta$ , supported on halfspace with material properties,  $G_h$  and  $\eta_h$

Figure 19. Dynamic stiffnesses of approach embankment of Meloland Road Overcrossing ( $G = 2.0MPa$ ,  $\eta = 0.52$ ). Spring and dashpot values are extracted by multiplying values shown above with width of embankment,  $B_c$ . Stiffness and damping values along longitudinal (y) direction are equal to those of transverse direction.

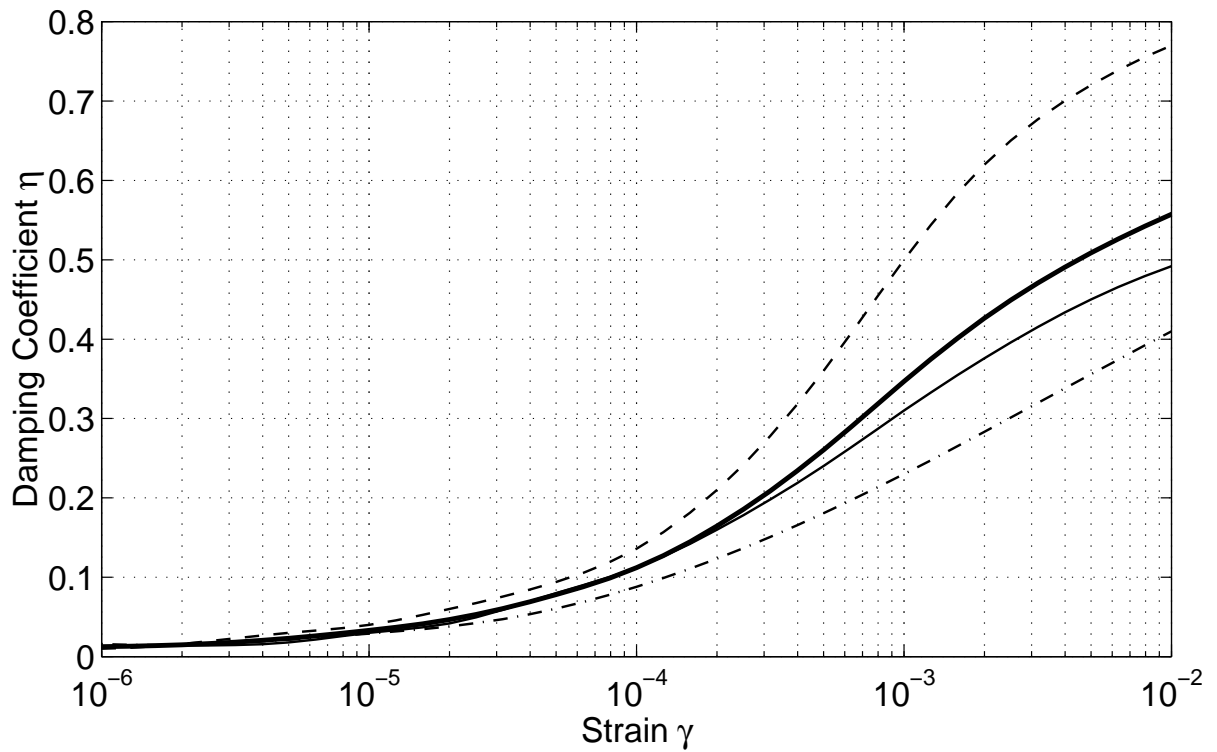
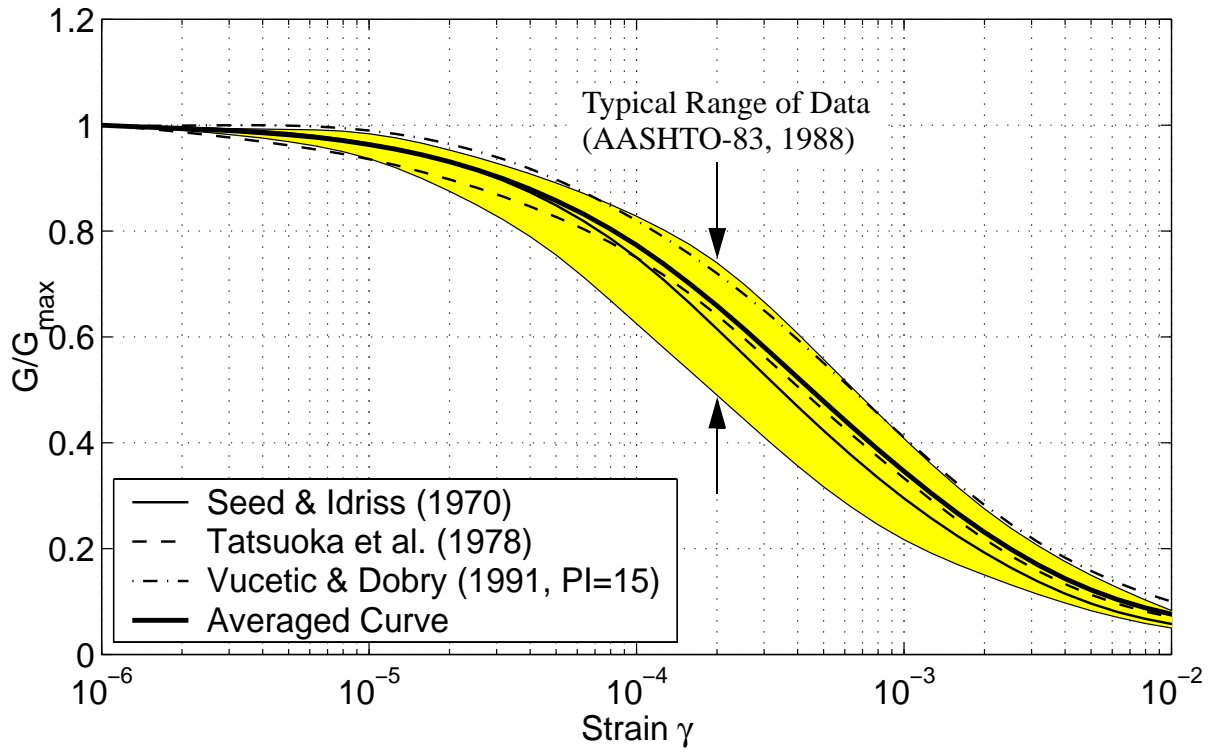
Figure 20. Dynamic stiffnesses of approaching embankment of Painter Street Bridge ( $G = 8.0MPa$ ,  $\eta = 0.50$ ). Spring and dashpot values are extracted by multiplying values shown above with width of embankment,  $B_c$ . Stiffness and damping values along longitudinal (y) direction are equal to those of transverse direction.

Figure 21. Free-body diagram of a section of a long embankment under transverse loading at one end

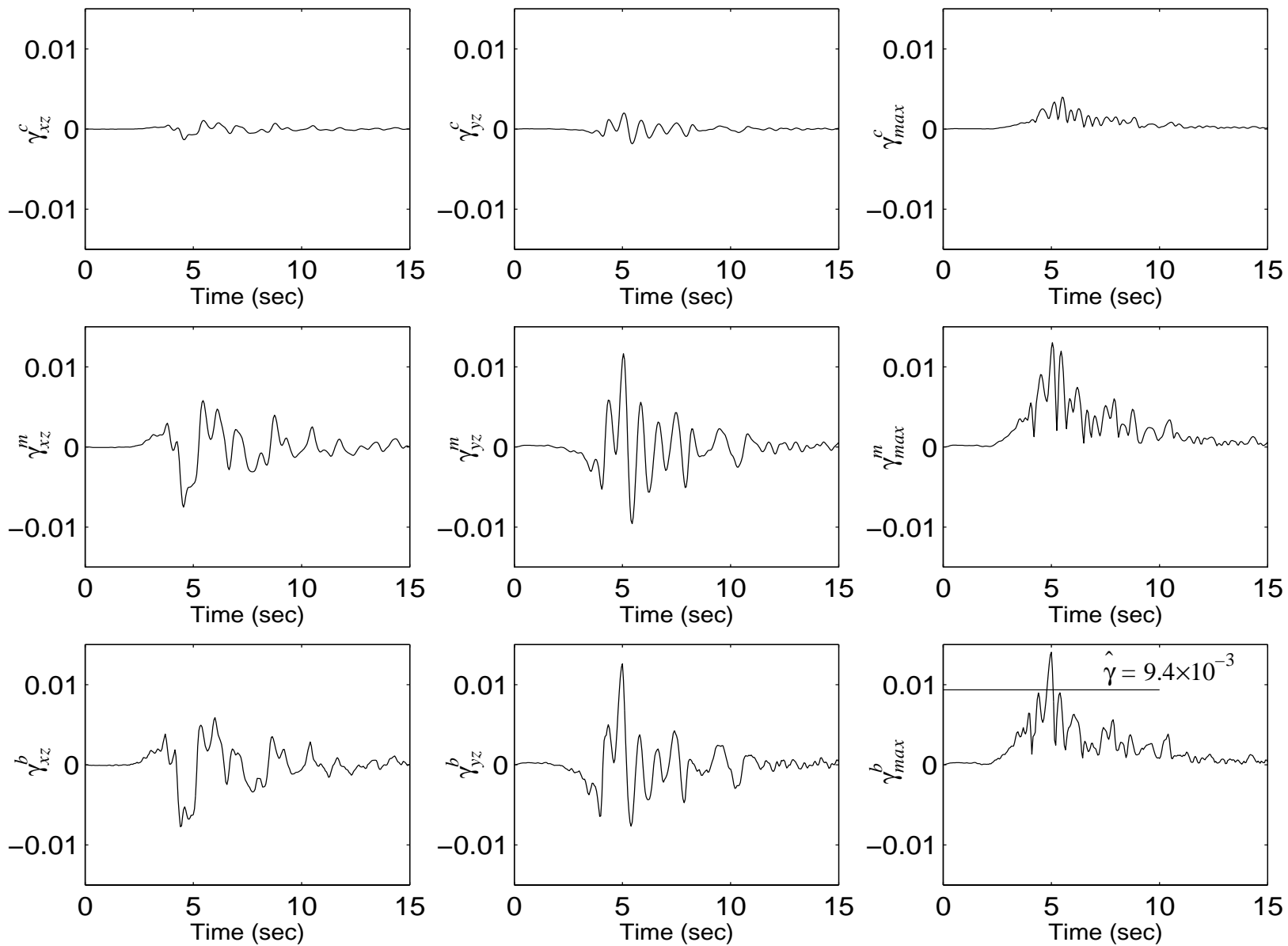
Figure 22. Critical-length parameter,  $\alpha = K_x / (\hat{k}_x \sqrt{SB_c H})$  for various geometries of approach embankment

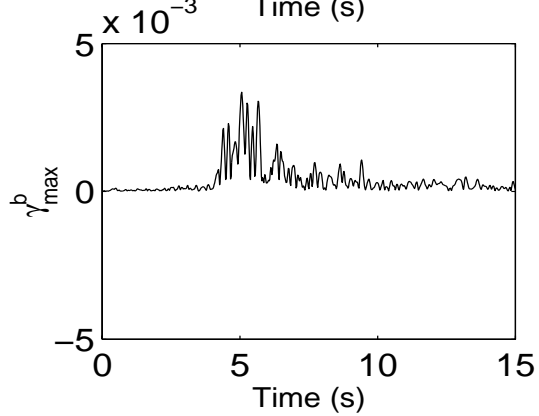
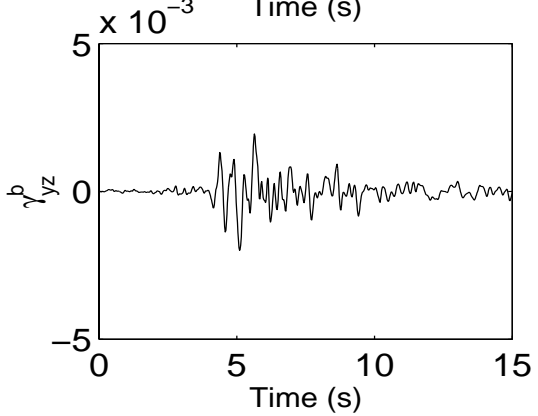
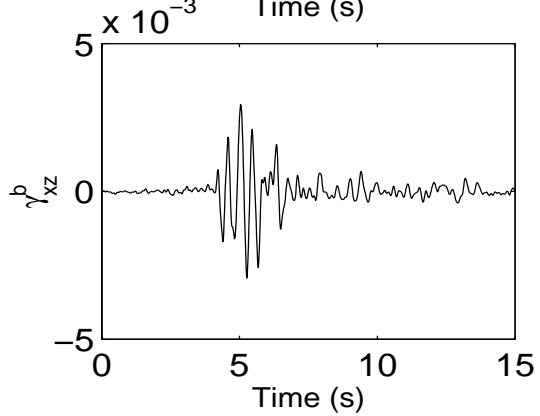
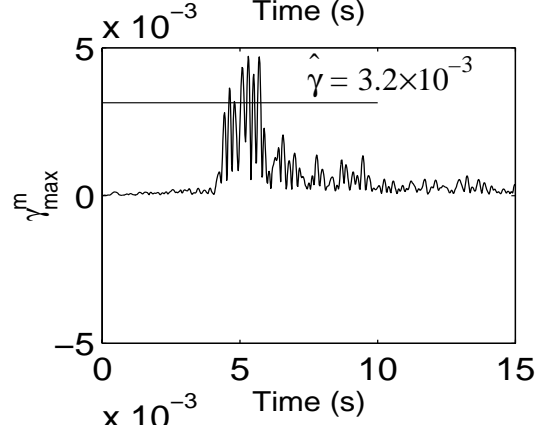
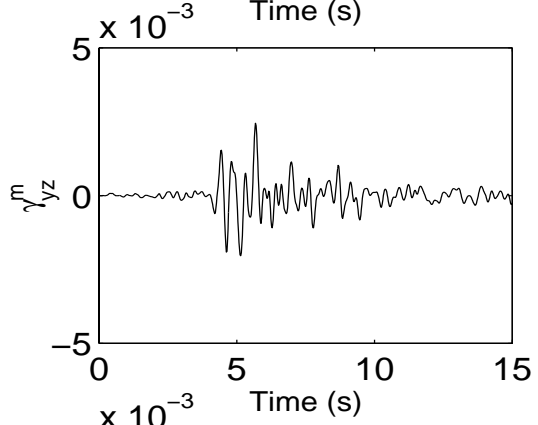
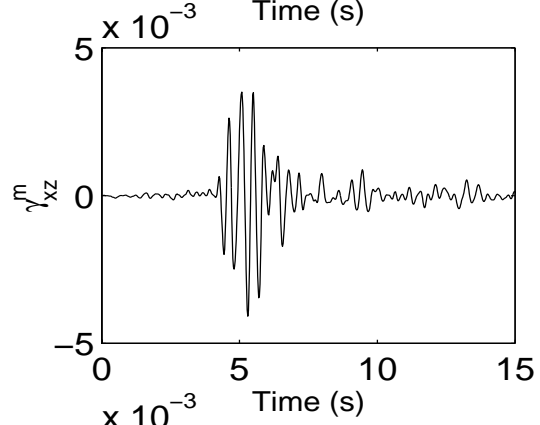
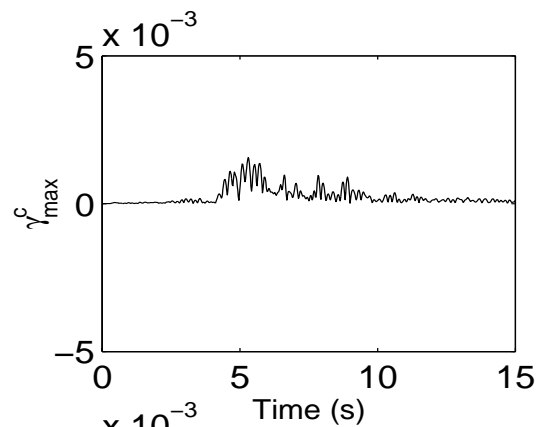
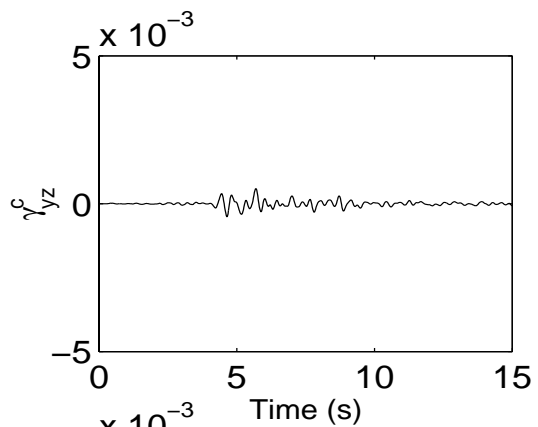
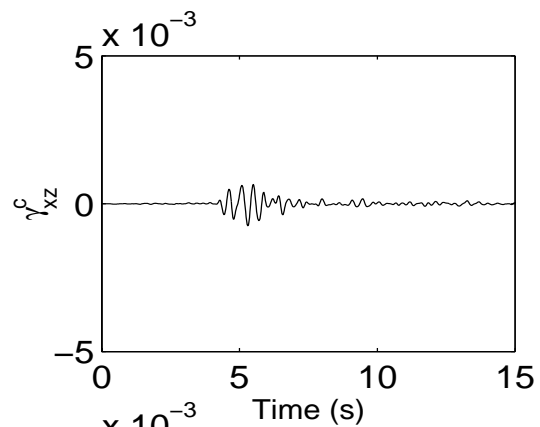


Geometry/Material Parameter	Meloland Road Overcrossing	Painter Street Overcrossing
$B_c$	34' (10.36 m)	50' (15.24 m)
$H$	26' (7.92 m)	31.5' (9.60 m)
$S$	1/2	1/2
$\rho_s$	1600 kg/m <sup>3</sup>	1600 kg/m <sup>3</sup>
$V_s$	110 m/s	190 m/s
Configuration	symmetric	symmetric

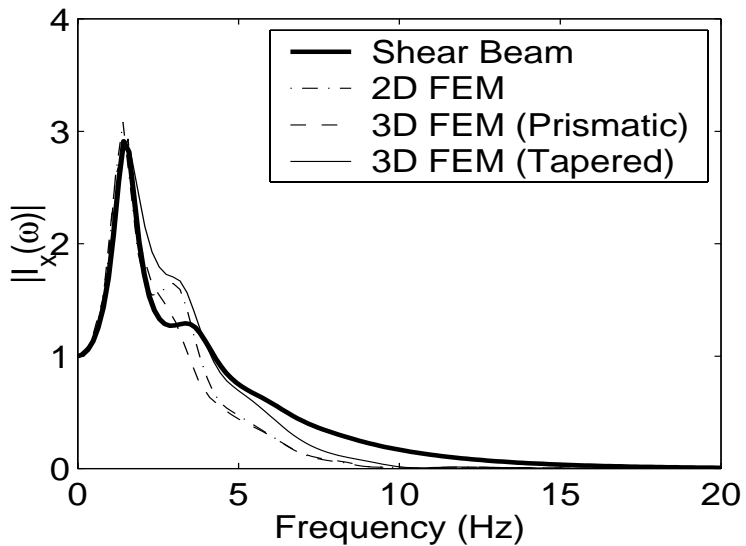




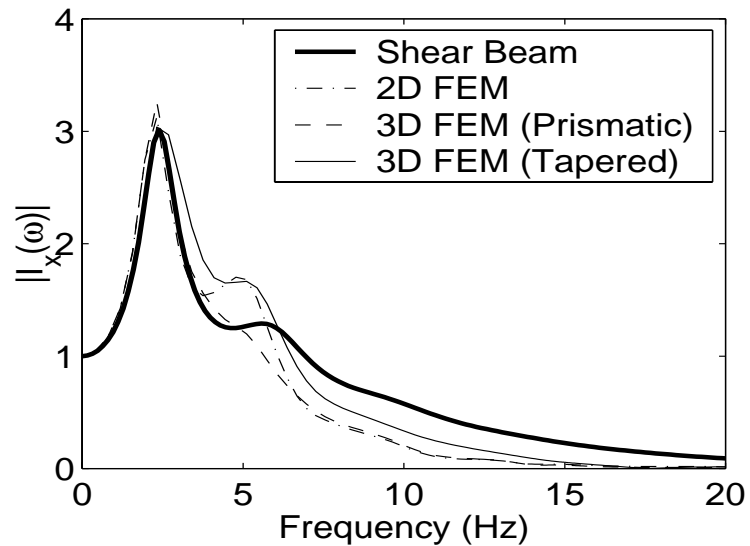




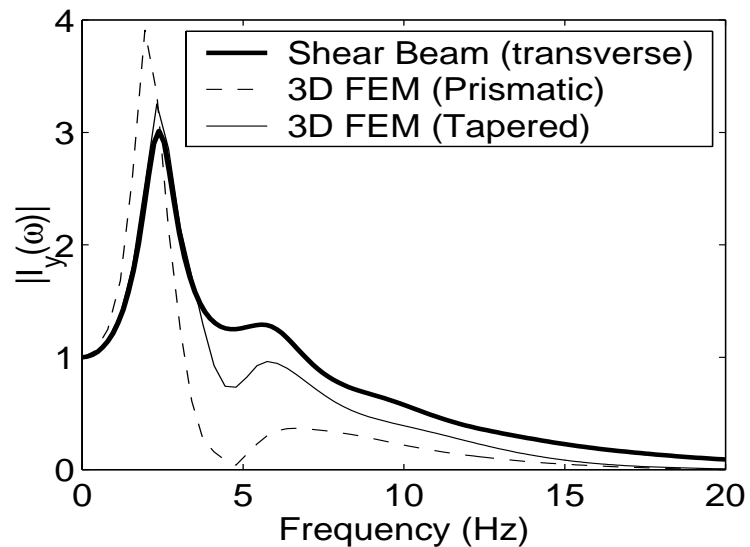
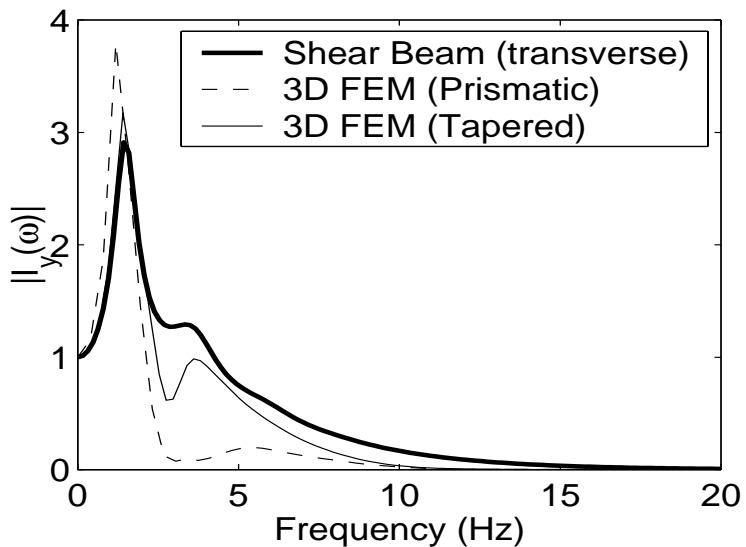
Meloland Overcrossing ( $G=2.0\text{MPa}$ ,  $\eta=0.52$ )

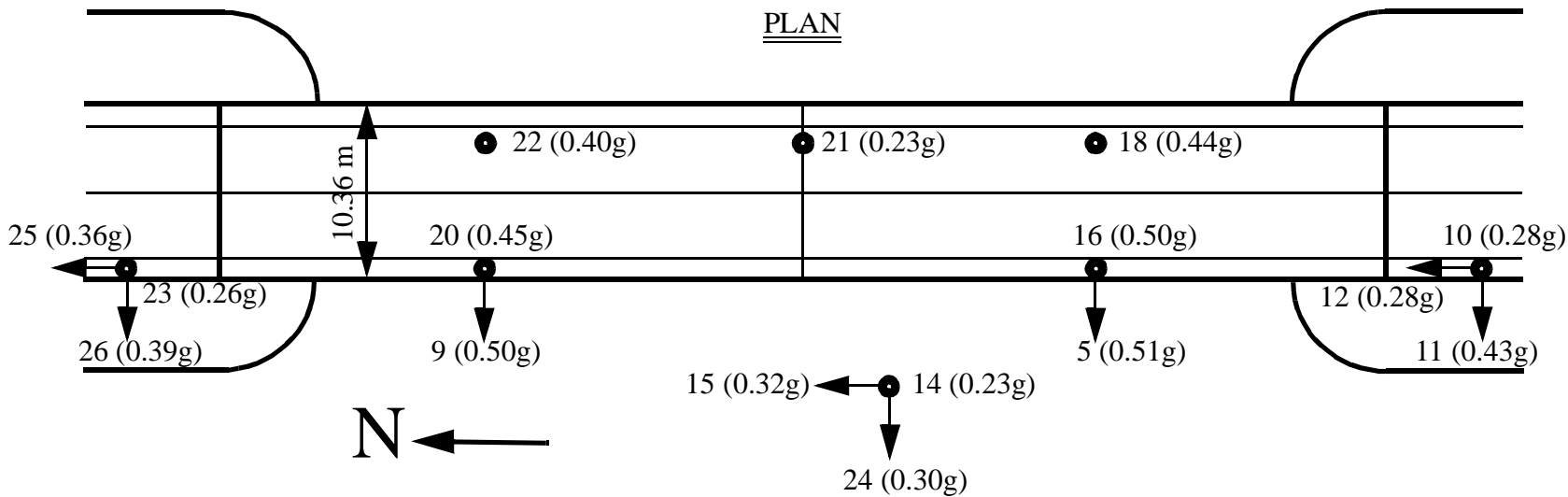
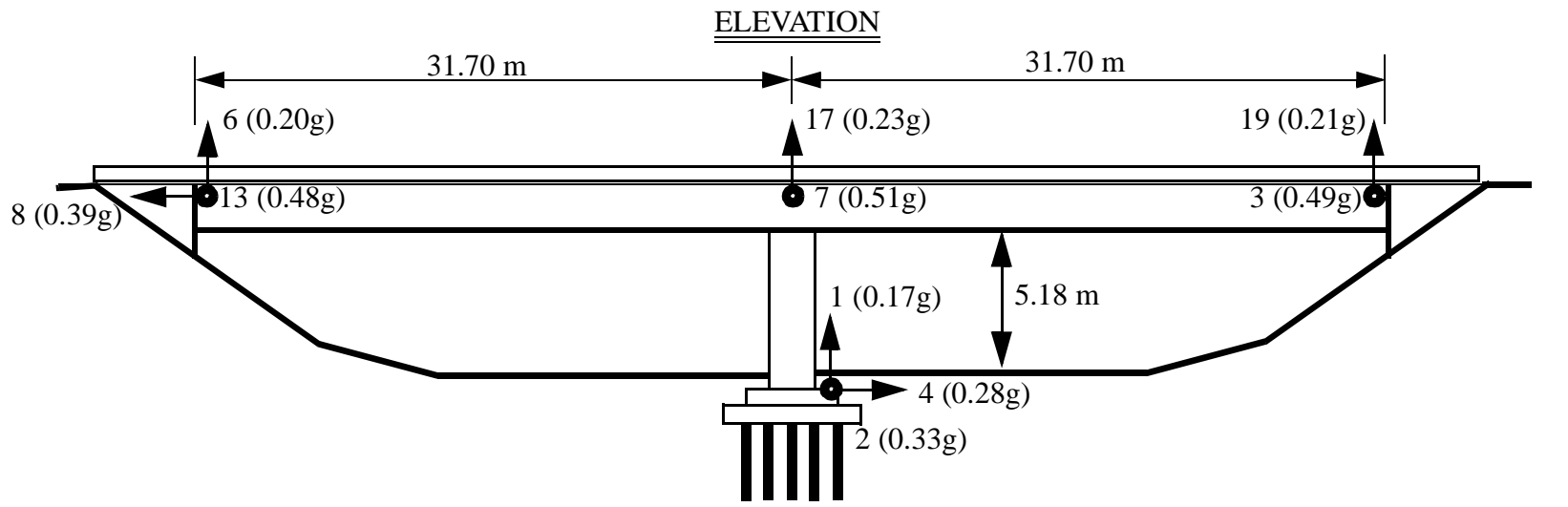


Painter Street Bridge ( $G=8.0\text{MPa}$ ,  $\eta=0.50$ )

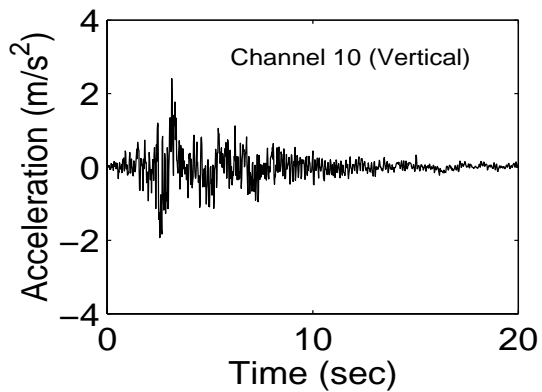
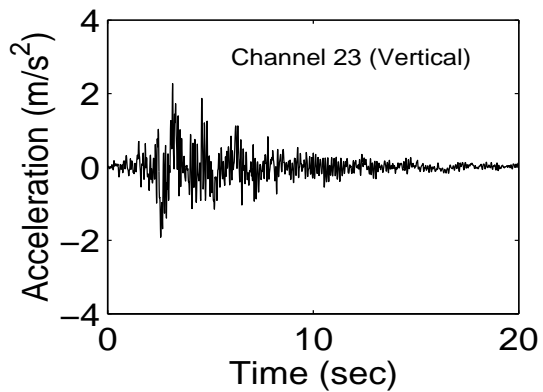
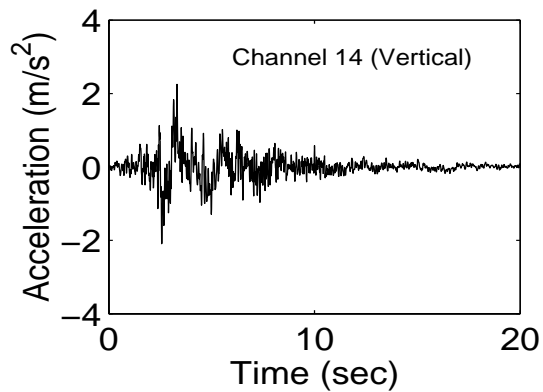
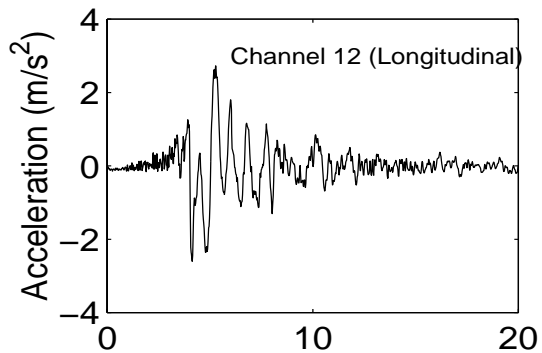
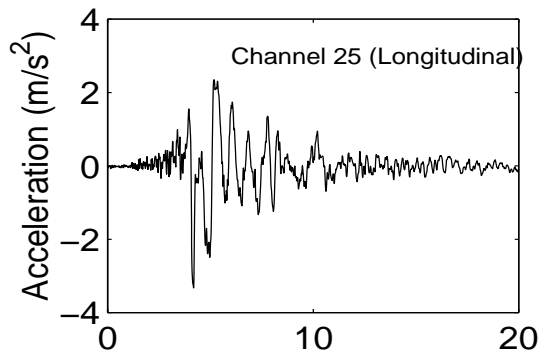
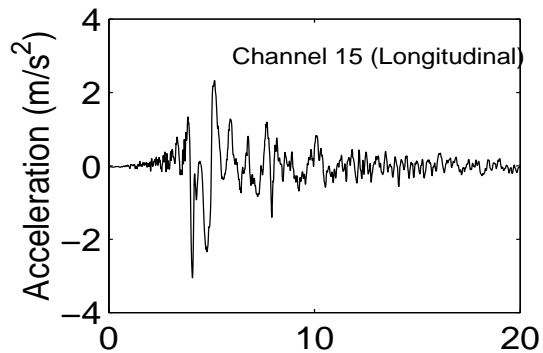
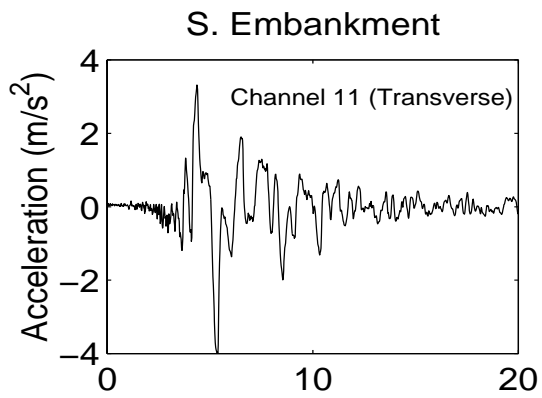
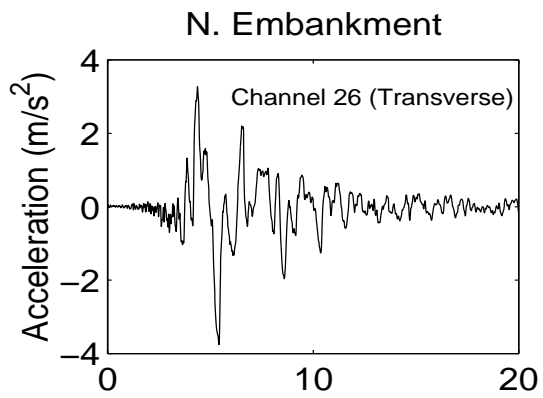
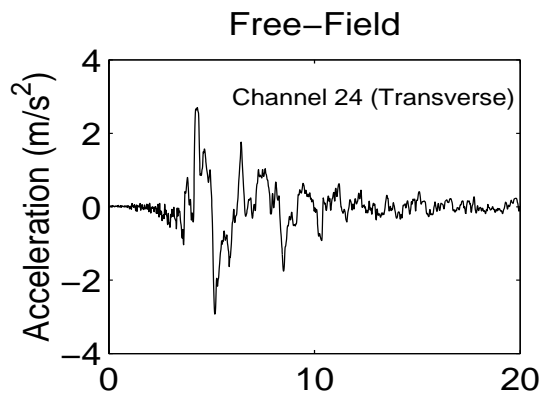


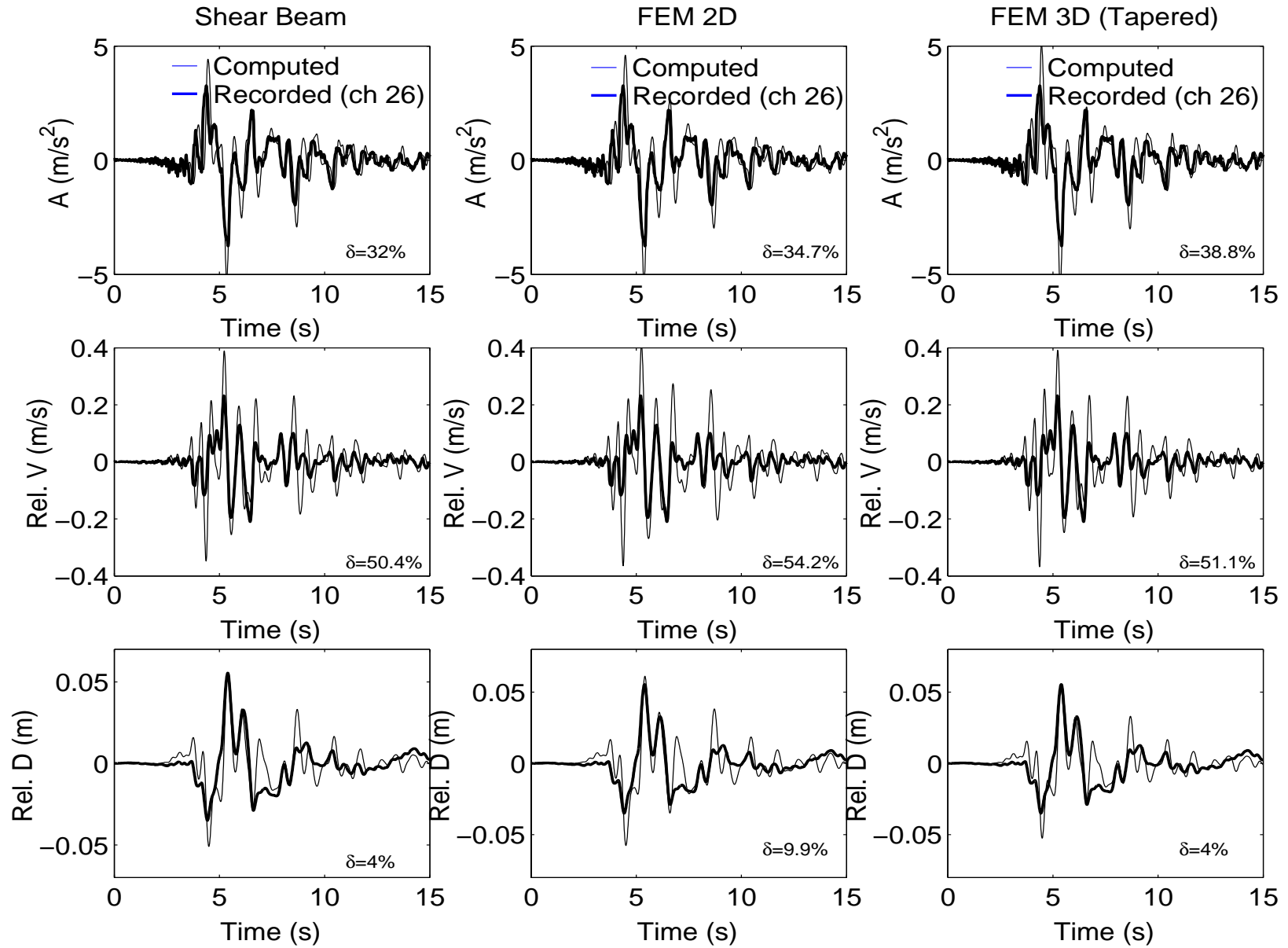
5

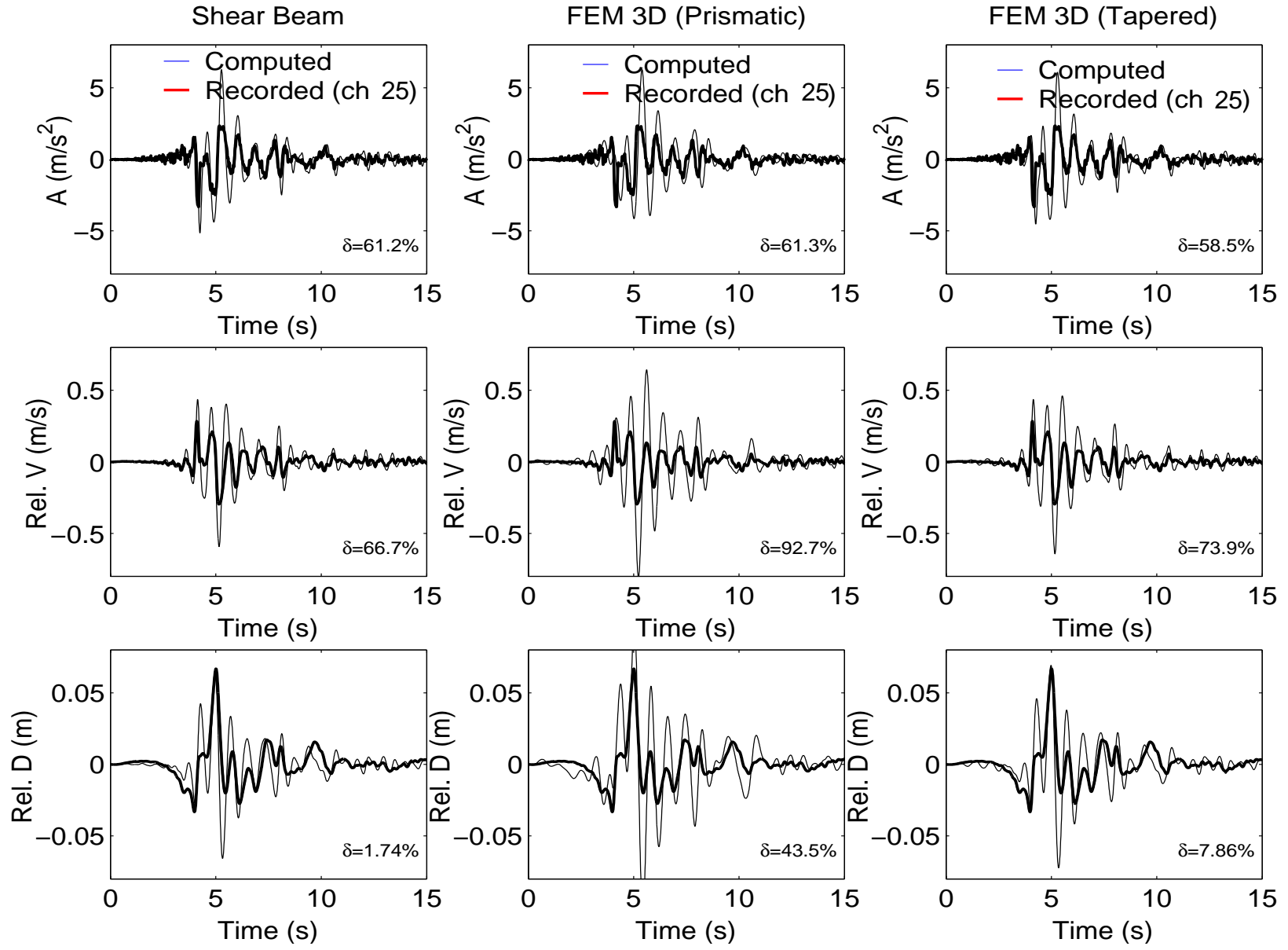


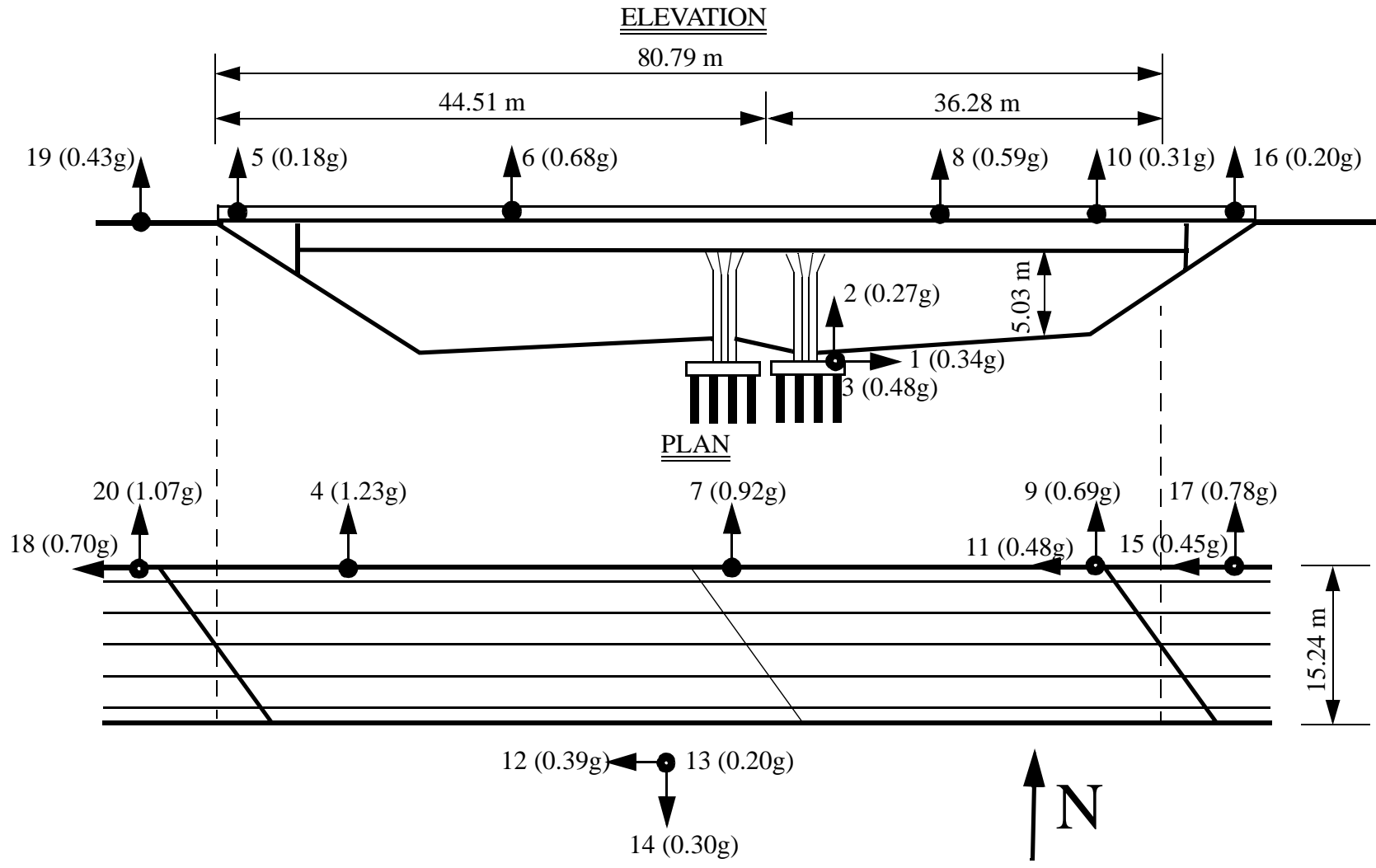


L

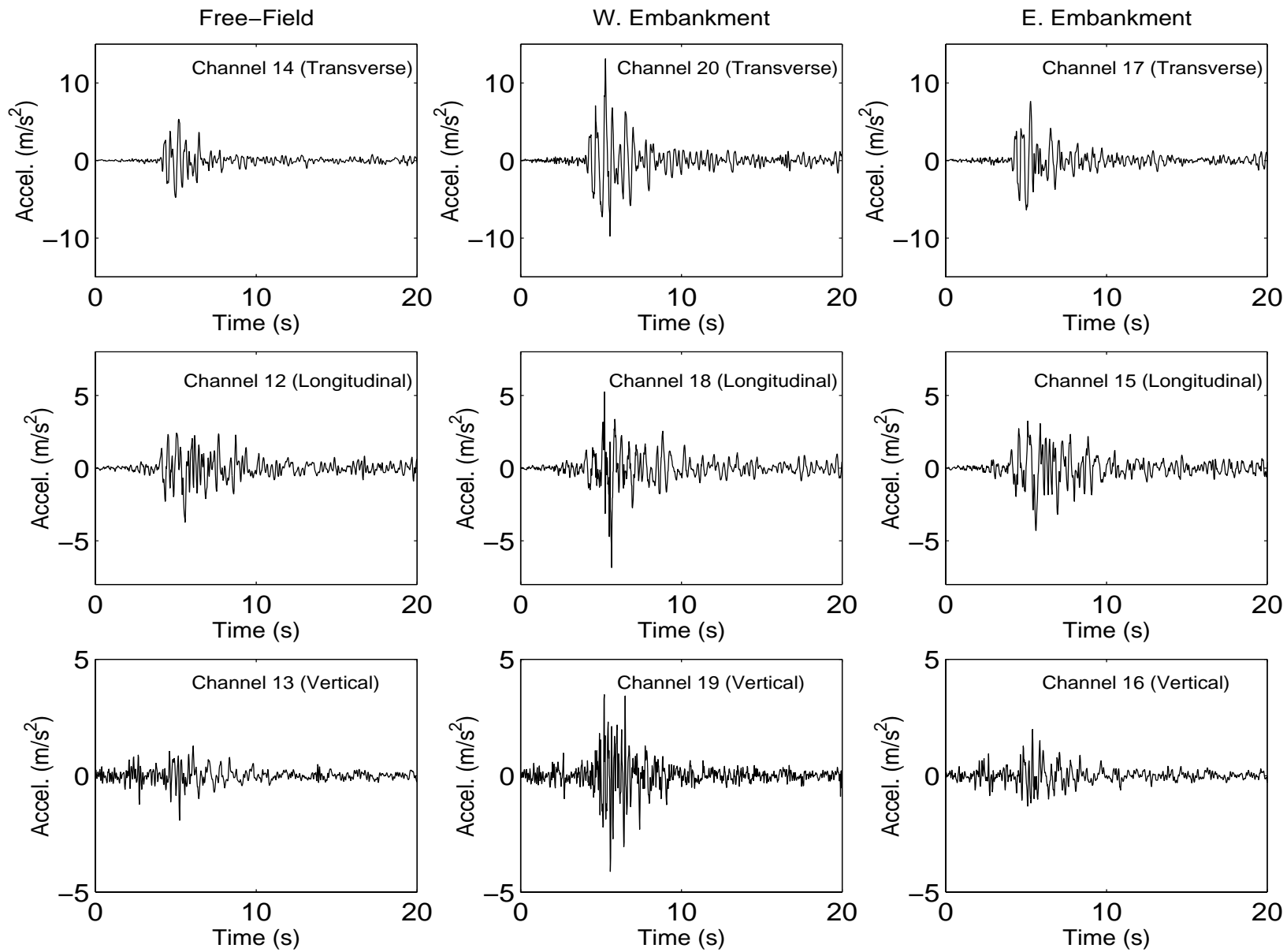


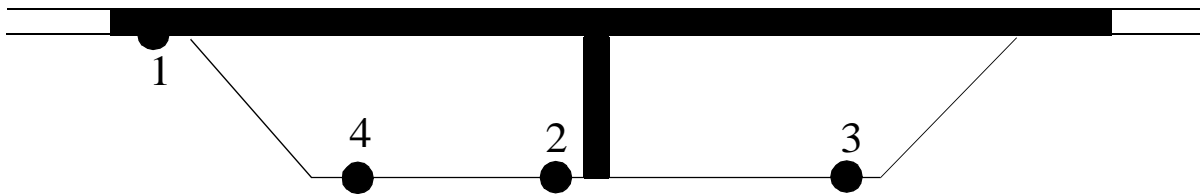




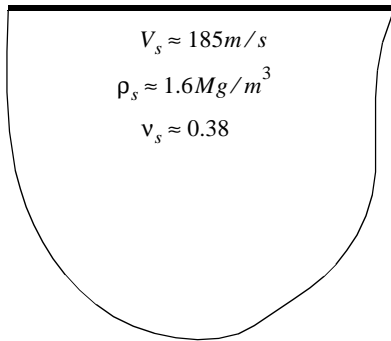




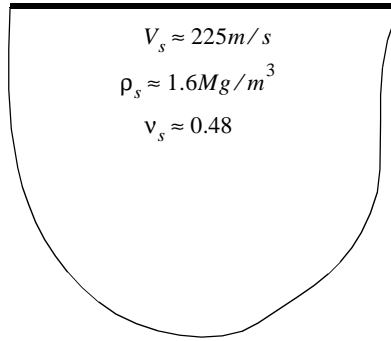




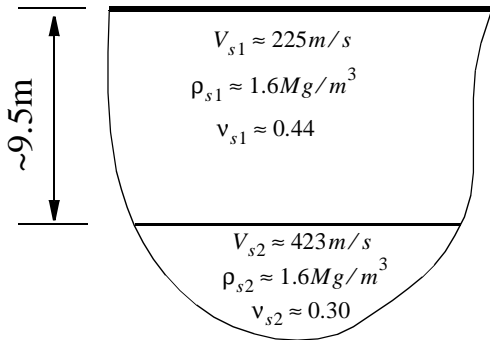
Line 1



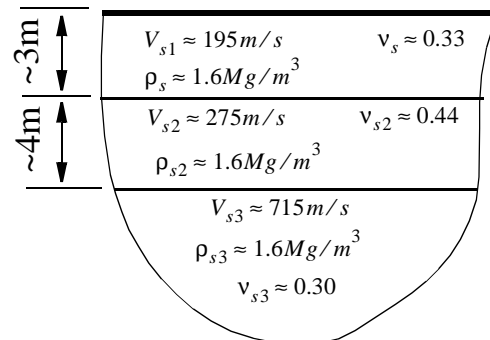
Line 2

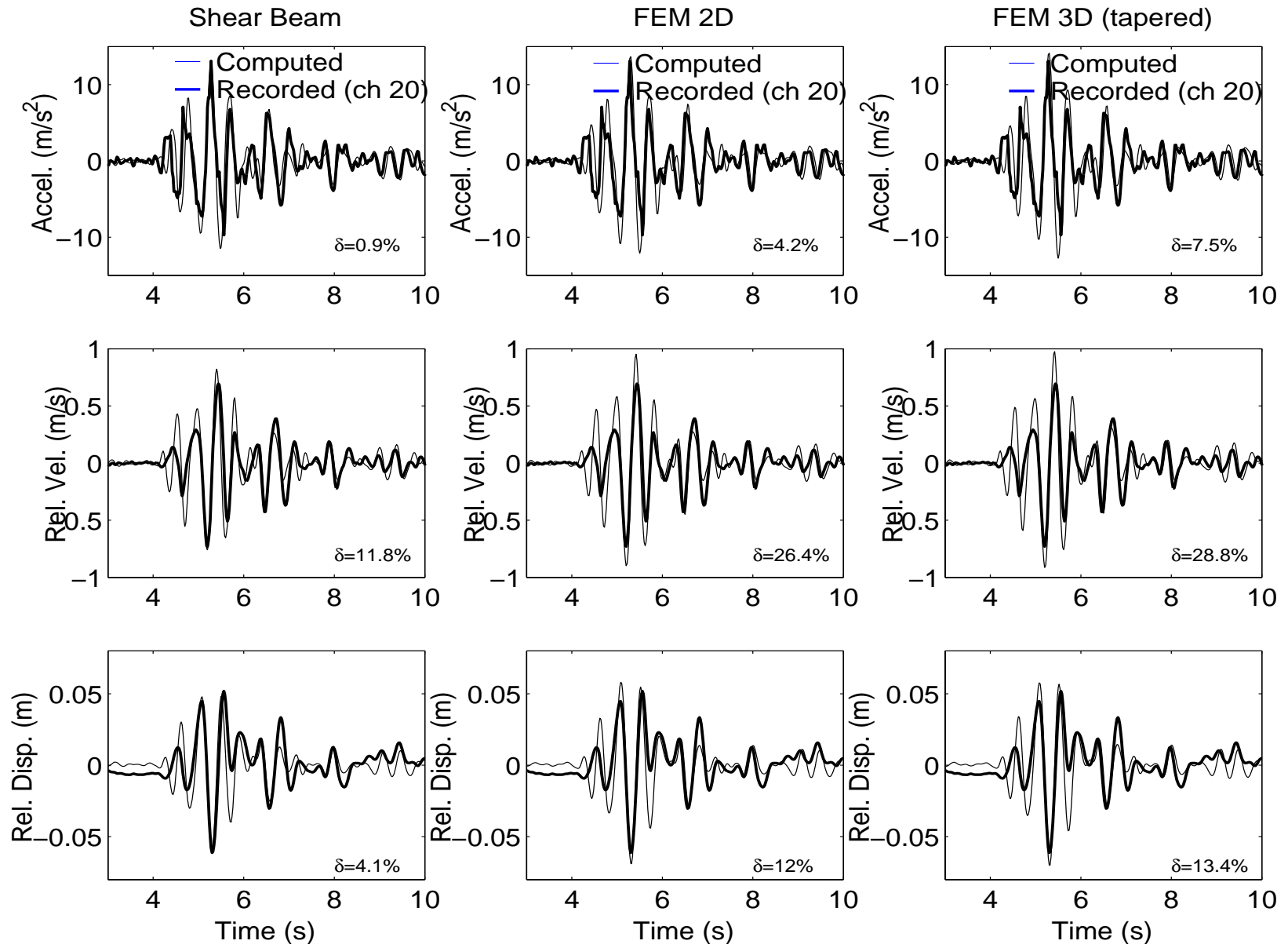


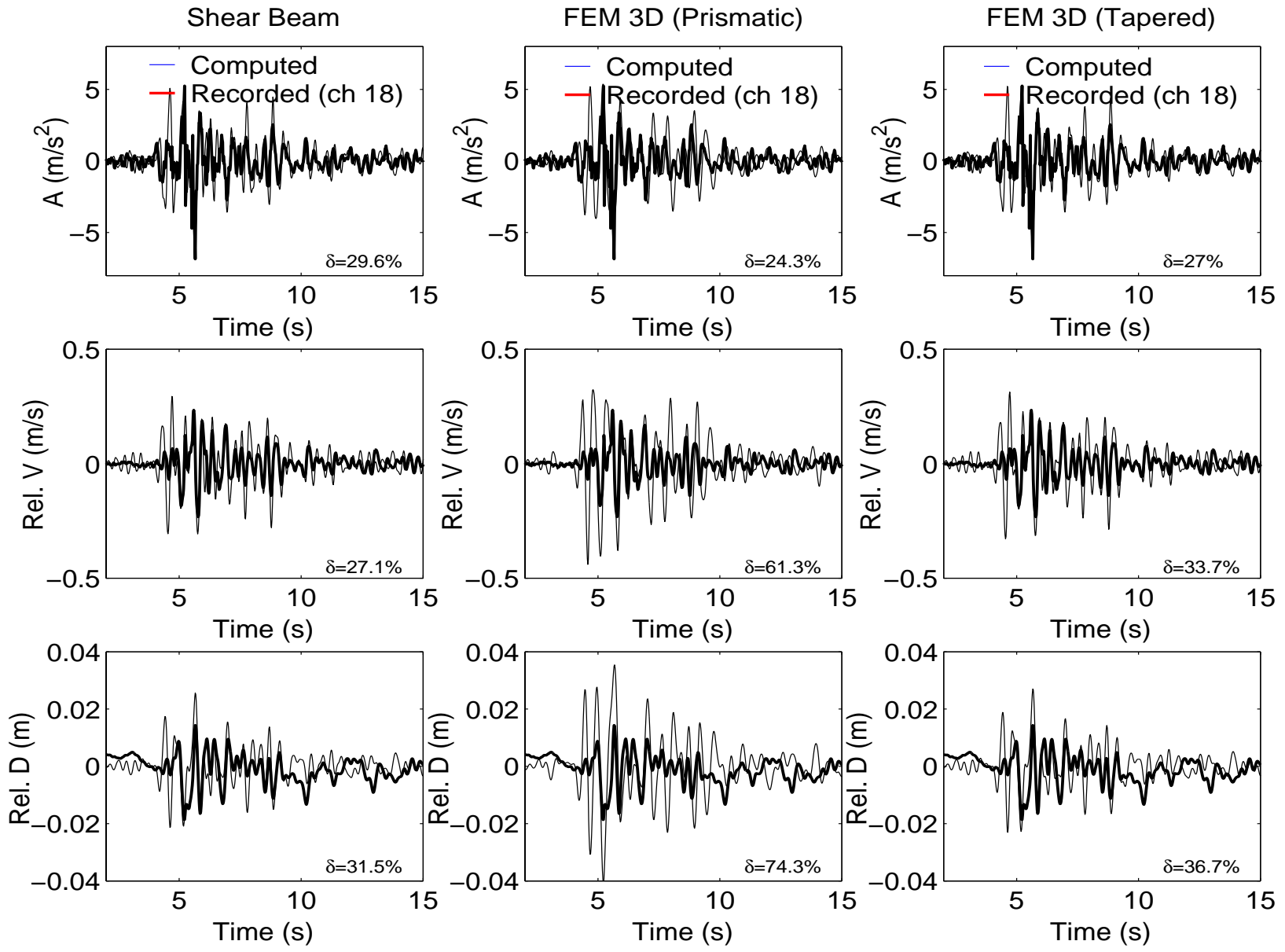
Line 3

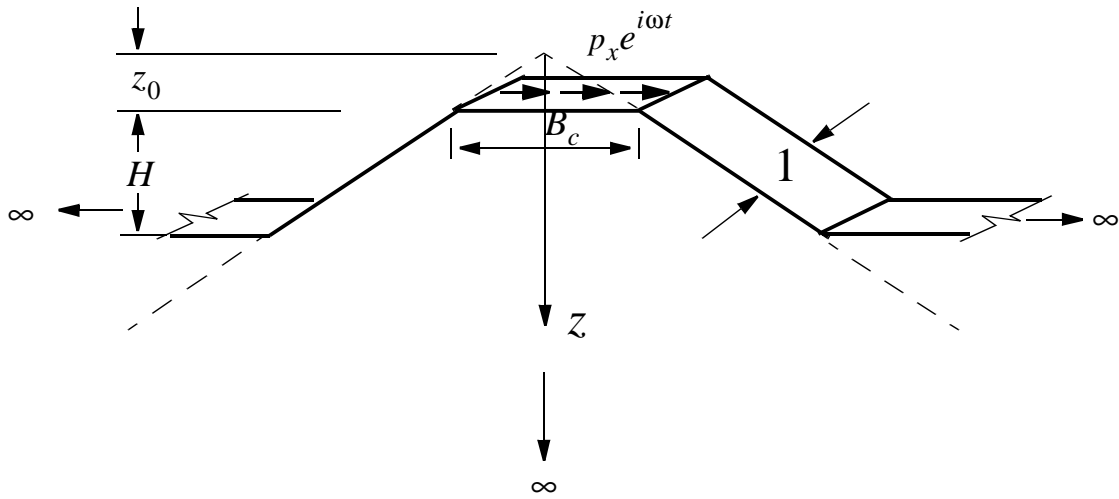
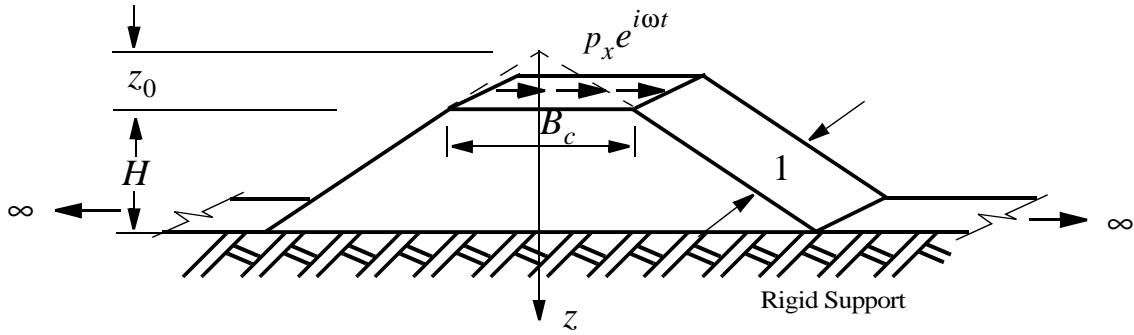


Line 4









Flexible Support — Infinite Wedge

